Monthly Notices of the ROYAL ASTRONOMICAL SOCIETY

MNRAS **511,** 6087–6109 (2022) https://doi.org/10.1093/mnras/stac110
Advance Access publication 2022 January 18

Planetary nebula luminosity function distances for 19 galaxies observed by PHANGS–MUSE

Fabian Scheuermann [1]★ Kathryn Kreckel [1] Gagandeep S. Anand [2,3] Guillermo A. Blanc [4,5] Enrico Congiu [5] Francesco Santoro [6] Schuyler D. Van Dyk [7] Ashley T. Barnes [8] Frank Bigiel [8] Simon C. O. Glover [9] Brent Groves [10] Ralf S. Klessen [9,11] J. M. Diederik Kruijssen [1] Erik Rosolowsky [12] Eva Schinnerer [6] Andreas Schruba,[13] Elizabeth J. Watkins [1] and Thomas G. Williams [6]

[1]*Astronomisches Rechen-Institut, Zentrum für Astronomie der Universität Heidelberg, Mönchhofstraße 12-14, D-69120 Heidelberg, Germany*
[2]*Space Telescope Science Institute, 3700 San Martin Drive, Baltimore, MD 21218, USA*
[3]*Institute for Astronomy, University of Hawaii, 2680 Woodlawn Drive, Honolulu, HI 96822, USA*
[4]*Observatories of the Carnegie Institution for Science, Pasadena, CA 91101, USA*
[5]*Departamento de Astronomía, Universidad de Chile, Casilla 36-D, Santiago, Chile*
[6]*Max-Planck-Institut für Astronomie, Königstuhl 17, D-69117 Heidelberg, Germany*
[7]*IPAC, California Institute of Technology, Pasadena, CA 91125, USA*
[8]*Argelander-Institut für Astronomie, Universität Bonn, Auf dem Hügel 71, D-53121 Bonn, Germany*
[9]*Universität Heidelberg, Zentrum für Astronomie, Institut für theoretische Astrophysik, Albert-Ueberle-Str. 2, D-69120 Heidelberg, Germany*
[10]*Research School of Astronomy and Astrophysics, Australian National University, Canberra, ACT 2611, Australia*
[11]*Universität Heidelberg, Interdisziplinäres Zentrum für Wissenschaftliches Rechnen, INF 205, D-69120 Heidelberg, Germany*
[12]*Department of Physics, University of Alberta, Edmonton, AB T6G 2E1, Canada*
[13]*Max-Planck-Institute for extraterrestrial Physics, Giessenbachstraße 1, D-85748 Garching, Germany*

Accepted 2022 January 12. Received 2022 January 11; in original form 2021 September 14

ABSTRACT

We provide new planetary nebula luminosity function (PNLF) distances to 19 nearby spiral galaxies that were observed with VLT/MUSE by the PHANGS collaboration. Emission line ratios are used to separate planetary nebulae (PNe) from other bright [O III] emitting sources like compact supernovae remnants (SNRs) or H II regions. While many studies have used narrowband imaging for this purpose, the detailed spectral line information provided by integral field unit (IFU) spectroscopy grants a more robust way of categorizing different [O III] emitters. We investigate the effects of SNR contamination on the PNLF and find that we would fail to classify all objects correctly, when limited to the same data narrowband imaging provides. However, the few misclassified objects usually do not fall on the bright end of the luminosity function, and only in three cases does the distance change by more than 1σ. We find generally good agreement with literature values from other methods. Using metallicity constraints that have also been derived from the same IFU data, we revisit the PNLF zero-point calibration. Over a range of $8.34 < 12 + \log(\mathrm{O/H}) < 8.59$, our sample is consistent with a constant zero-point and yields a value of $M^* = -4.542^{+0.103}_{-0.059}$ mag, within 1σ of other literature values. MUSE pushes the limits of PNLF studies and makes galaxies beyond 20 Mpc accessible for this kind of analysis. This approach to the PNLF shows great promise for leveraging existing archival IFU data on nearby galaxies.

Key words: galaxies: distances and redshifts – ISM: supernova remnant – planetary nebulae: general.

1 INTRODUCTION

Observations are the primary way to gather data in astronomy, but not all information is directly accessible. The measurement of some properties, like the intrinsic luminosity or the physical size of galaxies or stars depend on their distances. It is therefore fundamental for our understanding of the Universe to know those distances, but measuring them is a delicate task. Cosmic distances span many orders of magnitude, which prohibits the use of a single distance measure and instead necessitates a combination of techniques – the so-called *cosmic distance ladder*. Unfortunately, flaws in the different rungs can propagate into large uncertainties for the most distant objects (Bernal, Verde & Riess 2016; Freedman 2021). It is therefore desirable to find techniques that are accurate and easily applicable to a large number of objects.

For nearby galaxies, the *tip of the red giant branch* (TRGB, e.g. Lee, Freedman & Madore 1993), *Cepheids* (e.g. Freedman et al. 2001), *Type Ia supernovae* (SNe Ia, e.g. Riess, Press & Kirshner 1996), and *Surface Brightness Fluctuations* (SBF, e.g. Tonry et al. 2001) are among the premier techniques used to obtain precise distances, but redundant methods are essential to check for systematic differences. Another method that can achieve similar precision is

★ E-mail: f.scheuermann@uni-heidelberg.de

the *planetary nebulae luminosity function* (PNLF). Ford & Jenner (1978) were among the first to realize that planetary nebulae (PNe) can be utilized to determine the distance to their host galaxy. A PN is the last breath of a dying intermediate mass star (2–8 $M_\odot$; Kwok 2005). During the final stages of its life, the star will expels its outer layers, which will then be ionized by the UV radiation of the exposed hot core. The low densities of the rarefied gas, enables a wealth of collisionally excited emission lines (Osterbrock & Ferland 2006). Even though many stars will go through this phase at the end of their lives, the actual number of PNe that we observe is rather small, because they only last for a few tens of thousands of years (Buzzoni, Arnaboldi & Corradi 2006).

Since the maximum absolute magnitude of all PNe is roughly constant across all galaxies, they can be used as standard candles. Jacoby (1989) and Ciardullo et al. (1989a) formulated an empirical luminosity function that made use of this luminosity cut-off and in doing so, laid the groundwork for how we measure distances with PNe to the present day. Since then, the PNLF has been established as a reliable method for obtaining distances to nearby galaxies up to ∼20 Mpc, with a precision better than 10 per cent (e.g. Ciardullo, Jacoby & Tonry 1993; Ferrarese et al. 2000b; Ciardullo et al. 2002; Feldmeier, Jacoby & Phillips 2007).

The PNLF also plays a special role in the cosmic distance ladder. To the best of our knowledge (though still lacking a good theoretical foundation, Ciardullo 2013), the bright end cut-off of the PNLF is invariant to changes in the local environment or the metallicity and is applicable to both spiral (Feldmeier, Ciardullo & Jacoby 1997) and elliptical galaxies (Ciardullo, Jacoby & Ford 1989b). This makes this method useful for testing and comparing other methods. Beyond their use as a distance indicator, PNe are also used to measure kinematics in the outer halo where measuring stellar kinematics directly is difficult (Hartke et al. 2017).

The greatest challenge in measuring the PNLF distance is to compile a clean catalogue of PNe. Due to their strong [O III] λ5007 emission (Schönberner et al. 2010), they are easily detectable, but it can be difficult to discriminate them from other nebular objects like H II regions or supernova remnants (SNR). Baldwin, Phillips & Terlevich (1981) showed that emission line ratios can be used to make this discrimination. To this end, narrowband imaging with a combination of an [O III] on-band and a wider off-band filter together with a filter centred around H α, are used to identify PNe.

In recent years, the emergence of powerful *integral field unit* (IFU) spectroscopy instruments has revolutionized the field (Kreckel et al. 2017; Spriggs et al. 2020, 2021; Roth et al. 2021). Their fields of view are large enough to detect a sufficient number of PNe in order to measure the PNLF. PNe trace the underlying stellar population and hence we expect many more PNe in the denser central regions. This means that we can potentially find more objects in a smaller field of view. However, the strong stellar continuum in this part of the galaxy also makes it difficult to detect them with narrowband imaging. With the full spectral information from the IFU, we can remove the continuum and search for PNe in regions that were previously inaccessible.

We use data that were observed for **P**hysics at **H**igh **A**ngular resolution in **N**earby **G**alaxie**S** (PHANGS[1]). This is a collaboration aimed at studying the baryon cycle within galaxies at high spatial resolution, sufficient to isolate and characterise individual molecular clouds and H II regions. One of the pillars of this project are optical IFU spectroscopy observations with the Multi Unit Spectroscopic Explorer (MUSE; Bacon et al. 2010) at the Very Large Telescope (VLT). The PHANGS–MUSE sample consists of 19 nearby spiral galaxies that are all roughly face-on, ranging in mass from $\log_{10}(M/M_\odot) = 9.4$ to 10.99 and star formation rate from $\log_{10}(SFR/M_\odot\ yr^{-1}) = -0.56$ to 0.88.

This paper has three objectives. The first aim is to test how susceptible narrowband imaging is to misclassifying SNRs as PNe. Kreckel et al. (2017) found that, in the case of the nearby spiral galaxy NGC 0628, contamination with SNRs can bias the measured distance. Meanwhile, Davis et al. (2018) could not find such problems for M 31 and M 33. The lingering question is whether NGC 0628 was just an anomaly or if this issue compromises other galaxies as well.

The second goal is to quantify the applicability of IFU surveys for PN studies. Past PN studies required special observations that were taken for the sole purpose of finding PNe. Because IFU studies cover the relevant emission lines anyway, this opens up the possibility of measuring the PNLF as a 'bonus'. The gain in versatility comes at a price: The fields of view are usually narrower. Here we try to quantify whether IFU surveys can compensate the smaller fields of view with a gain in spectral information and explorer the limitations to derive PNLF-based distances from IFU observations.

The last objective is to provide new and precise distance measurements for the 19 nearby galaxies observed by the PHANGS–MUSE survey, some of which did not have good distance estimates before. In Section 2, we present the data that is used for this study and describe our process for identifying PNe. In Section 3, we fit the observed data to the PNLF and in Sections 4 and 5 we present and discuss the results. We conclude in Section 6.

2 FINDING PLANETARY NEBULAE

We begin by compiling a clean catalogue of PN candidates followed by a second catalogue with potential SNR contaminants that might be misclassified in narrowband studies.

2.1 Data

We use the full sample of 19 nearby spiral galaxies (see Table 1) that were observed with VLT/MUSE for the PHANGS–MUSE large observing program (PI: Schinnerer; Emsellem et al. 2021). The wide-field mode of MUSE has a field of view of 1×1 arcmin^2 and only covers part of the targeted galaxies. Between 3 and 15 pointings were taken to sample the bulk of the star-forming disc of each target. The observations cover a wavelength range from 4800 to 9300 Å, with a typical spectral resolution of 2.75 Å. Each pixel covers 0.2×0.2 arcsec^2 with an average spatial resolution of 0.72 arcsec (67 pc).

The data reduction was performed by the PHANGS–MUSE team, using the MUSE data processing pipeline by Weilbacher et al. (2020), and is described in Emsellem et al. (2021). They produced reduced and mosaicked spectral cubes that form the base for further data analysis pipeline (DAP) products which we use for our analysis. This includes emission line maps that are extracted by fitting Gaussian profiles along with the stellar continuum. We use those maps for the H β λ4861, H α λ6562, [N II] λ6583, [S II] λ6716, and [S II] λ6731 emission lines. We also use the [O III] λ5007 line maps, which are not tied to any of the other lines during the fit, for PN source detection. For our analysis, we use the native resolution DAP maps from the public data release 1.0.

However, this procedure is not suitable to obtain accurate [O III] λ5007 fluxes. [O III] emission is mostly associated with

[1] http://www.phangs.org

Table 1. Properties of the galaxies in the PHANGS–MUSE sample.

Name	Type	R.A. (J2000)	Dec. (J2000)	$(m-M)^a$ mag	i^b deg	PA^b deg	r_{25} arcmin	$12+\log(\mathrm{O/H})^c$	$E(B-V)^d$	FWHM^e arcsec
IC 5332	SABc	$23^h34^m27\overset{s}{.}49$	$-36^d06^m03\overset{s}{.}89$	29.77 ± 0.10	26.9	74.4	3.03	8.38	0.015	0.72^{AO}
NGC 0628	Sc	$01^h36^m41\overset{s}{.}73$	$+15^d47^m01\overset{s}{.}11$	29.96 ± 0.14	8.9	20.7	4.94	8.50	0.062	0.73^{AO}
NGC 1087	Sc	$02^h46^m25\overset{s}{.}18$	$-00^d29^m55\overset{s}{.}38$	31.00 ± 0.30	42.9	359.1	1.49	8.37	0.030	0.74^{AO}
NGC 1300	Sbc	$03^h19^m41\overset{s}{.}00$	$-19^d24^m40\overset{s}{.}01$	31.39 ± 0.33	31.8	278.0	2.97	8.52	0.026	0.63
NGC 1365	Sb	$03^h33^m36\overset{s}{.}36$	$-36^d08^m25\overset{s}{.}45$	31.46 ± 0.09	55.4	201.1	6.01	8.54	0.018	0.82^{AO}
NGC 1385	Sc	$03^h37^m28\overset{s}{.}56$	$-24^d30^m04\overset{s}{.}18$	31.18 ± 0.33	44.0	181.3	1.70	8.40	0.018	0.49
NGC 1433	SBa	$03^h42^m01\overset{s}{.}49$	$-47^d13^m18\overset{s}{.}99$	29.78 ± 0.49	28.6	199.7	3.10	8.55	0.008	0.65
NGC 1512	Sa	$04^h03^m54\overset{s}{.}14$	$-43^d20^m55\overset{s}{.}41$	30.28 ± 0.33	42.5	261.9	4.22	8.56	0.009	0.8^{AO}
NGC 1566	SABb	$04^h20^m00\overset{s}{.}38$	$-54^d56^m16\overset{s}{.}84$	31.24 ± 0.25	29.5	214.7	3.61	8.55	0.008	0.64
NGC 1672	Sb	$04^h45^m42\overset{s}{.}49$	$-59^d14^m50\overset{s}{.}13$	31.44 ± 0.33	42.6	134.3	3.08	8.54	0.021	0.72^{AO}
NGC 2835	Sc	$09^h17^m52\overset{s}{.}91$	$-22^d21^m16\overset{s}{.}84$	30.44 ± 0.17	41.3	1.0	3.21	8.38	0.089	0.85^{AO}
NGC 3351	Sb	$10^h43^m57\overset{s}{.}76$	$+11^d42^m13\overset{s}{.}21$	29.99 ± 0.07	45.1	193.2	3.61	8.59	0.024	0.74^{AO}
NGC 3627	Sb	$11^h20^m15\overset{s}{.}00$	$+12^d59^m29\overset{s}{.}40$	30.27 ± 0.09	57.3	173.1	5.14	8.55	0.037	0.77^{AO}
NGC 4254	Sc	$12^h18^m49\overset{s}{.}63$	$+14^d24^m59\overset{s}{.}08$	30.59 ± 0.33	34.4	68.1	2.52	8.53	0.035	0.58
NGC 4303	Sbc	$12^h21^m54\overset{s}{.}93$	$+04^d28^m25\overset{s}{.}48$	31.15 ± 0.39	23.5	312.4	3.44	8.56	0.020	0.58
NGC 4321	SABb	$12^h22^m54\overset{s}{.}93$	$+15^d49^m20\overset{s}{.}29$	30.91 ± 0.07	38.5	156.2	3.05	8.56	0.023	0.64
NGC 4535	Sc	$12^h34^m20\overset{s}{.}30$	$+08^d11^m52\overset{s}{.}70$	30.99 ± 0.05	44.7	179.7	4.07	8.55	0.017	0.44
NGC 5068	Sc	$13^h18^m54\overset{s}{.}74$	$-21^d02^m19\overset{s}{.}48$	28.58 ± 0.09	35.7	342.4	3.74	8.34	0.091	0.73^{AO}
NGC 7496	Sb	$23^h09^m47\overset{s}{.}29$	$-43^d25^m40\overset{s}{.}26$	31.36 ± 0.33	35.9	193.7	1.67	8.51	0.008	0.79

Notes. Adopted from the PHANGS sample table (v1p6, see Leroy et al. 2021).
[a]Curated by Anand et al. (2021). For NGC 1433 and NGC 1512 the distances are from Sabbi et al. (2018).
[b]Inclination and position angle from Lang et al. (2020).
[c]At the mean positions of the PNe with gradients from Kreckel et al. (2020) and Santoro et al. (2022).
[d]Galactic foreground extinction from Schlafly & Finkbeiner (2011).
[e]Average FWHM of the PSF across all pointings. Galaxies that were observed with adaptive optics are marked with AO.

certain objects like PNe, SNRs, and H II regions, and most parts of a galaxy will have little to no emission. By fitting a Gaussian profile in a region without emission, we create a positive bias. To circumvent this issue, we calculate the non-parametric emission-line moment for [O III] λ5007 following the procedure employed in the MaNGA data analysis pipeline (Belfiore et al. 2019; Westfall et al. 2019). We use the velocity from the Hα line to calculate the expected rest-frame wavelength of the [O III] line and sum the flux over 17 spectral bins, corresponding to a wavelength range of 4998–5018 Å. This range is wide enough to ensure that we always capture the [O III] line, even in the case that the velocity from the Hα is off. In a similar way, the continuum is measured in the range from 4978 to 4998 Å and 5018 to 5038 Å with three sigma clipping and then subtracted from the line flux.

In order to measure the flux of a point source like a PN, one needs to know the shape of the point spread function (PSF). For our MUSE data, it is best parametrized by a Moffat profile (Bacon et al. 2017; Fusco et al. 2020)

$$p(r) = A\left[1+\left(\frac{r^2}{\gamma^2}\right)\right]^{-\alpha}. \quad (1)$$

A fixed power index of $\alpha = 2.3$ is used for galaxies with adaptive optics (AO) observations and $\alpha = 2.8$ for the remaining galaxies (both values were provided by ESO). The core width γ varies from pointing to pointing and is related to the full width half maximum via $\mathrm{FWHM} = 2\gamma\sqrt{2^{1/\alpha}-1}$. The latter is usually measured from bright point-like objects. However, since many pointings in our data do not have such objects, we use a different approach where we measure the FWHM with the help of a reference image with a known PSF (Emsellem et al. 2021). Unfortunately, the derived FWHM can have a rather large uncertainties of up to 0.1 arcsec. The FWHM is measured at a reference wavelength of 6483.58 Å and it decreases linearly with increasing wavelength. This can be approximated with

$$\mathrm{FWHM}(\lambda) = \mathrm{FWHM}_{\mathrm{ref}} - 3\times10^{-5}\,\mathrm{arcsec\,\AA^{-1}}(\lambda - 6483.58\,\mathrm{\AA}), \quad (2)$$

where $\mathrm{FWHM}_{\mathrm{ref}}$ is measured at the reference wavelength.

2.2 Source detection and photometry

To create an initial catalogue of PNe candidates, we use a four step procedure: First, we search for unresolved objects in the Gaussian fit [O III] line map. Then, we measure their fluxes within the non-parametric moment 0 maps with aperture photometry and subtract the background from an annulus. Next, we correct for the flux that is lost outside of the aperture and finally apply a correction for Milky Way extinction.

The physical resolution of the observations varies between 25 and 95 pc (based on prior distances from Anand et al. 2021). This means that PNe, which typically have sizes of less than 1 pc (Bojičić et al. 2021), will always appear as unresolved objects. For the bright PNe that are of interest to us, the strongest emission line is the forbidden [O III] λ5007 line, so we search for point sources in this line map (see Fig. 1). Before we start with the source finding, we mask out regions around known stars from *GAIA* DR2 (Gaia Collaboration 2018) to account for foreground objects. Other problematic regions are the centres of galaxies with strong [O III] emission. This can lead to other objects being mistakenly classified as PNe. To avoid this, we create an elliptical mask and place it at the galaxy centre. We select a semi-major-axis of $0.2 \cdot r_{25}$. This allows us to reliable get rid of most problematic objects. We also mask the parts of the image that have Hα fluxes above the 95th percentile of the entire image. This removes some parts of the spiral arms. This problem only concerns some of the galaxies in our sample and we only apply this treatment to the following galaxies: NGC 1300, NGC 1365, NGC 1512, NGC 1566, NGC 1672,

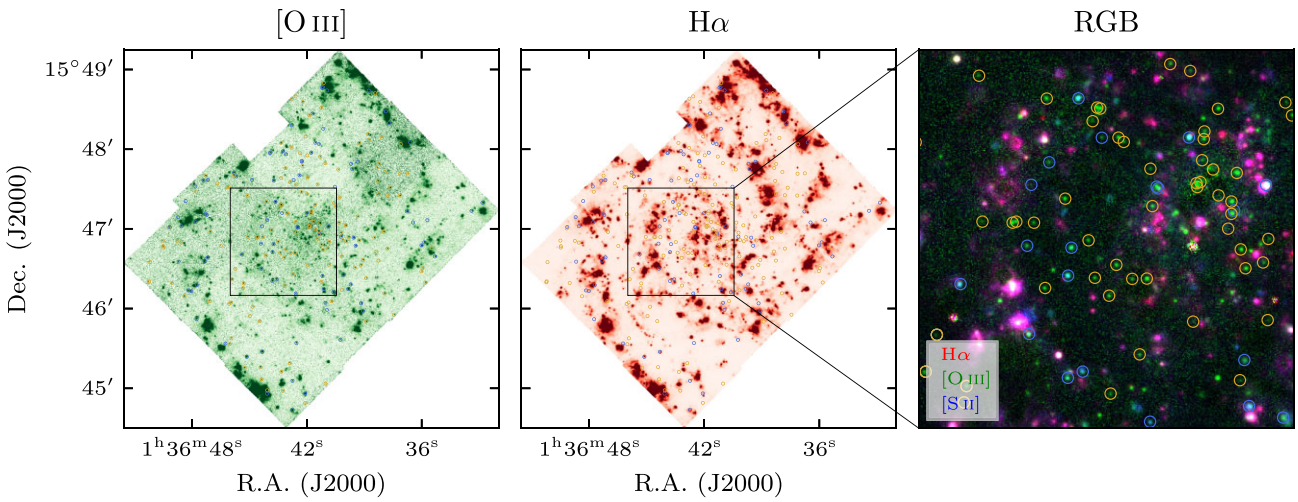

Figure 1. Mapping the location of emission lines sources in NGC 628. PNe (marked with gold circles) appear as bright point like objects in the [O III] map (left). Objects that also show significant H α emission (centre) are often other objects like H II regions or SNRs (marked with blue circles). In the composite RGB image (right), PNe stand out as bright green dots.

NGC 3351, NGC 3627 NGC 4303, NGC 4321, NGC 4535, and NGC 7496. Between 6.5 to 13.6 per cent of the fields of view are masked in the process.

The source detection itself is performed with the Python package PHOTUTILS (Bradley et al. 2019) which provides an implementation of the DAOPHOT algorithm from Stetson (1987). Because individual pointings differ slightly in noise and PSF size, we process them individually. For each of them, the noise level is estimated from the standard deviation with iterative three sigma clipping. We then search for objects above a threshold of 3 times this noise level. This constitutes our preliminary catalogue of PN candidates.

The next step is to measure the fluxes, which is done with aperture photometry. A smaller aperture is generally favourable because it only uses the brightest part of the object and hence increases the signal to noise (Howell 1989). However, this requires a good knowledge of the PSF. Because we are not able to get a precise measurement of the PSF in each pointing (see Emsellem et al. 2021, for a detailed discussion of the PSF), those errors would then propagate into the measured fluxes. We therefore use a rather large aperture with a diameter of 2.5 · FWHM. Only with this large aperture size does the uncertainty due to the PSF reach a level similar to that of the photometric error (≈ 0.1 mag).

The background is estimated from an annulus, with the inner radius set to 4 · FWHM and the outer radius chosen such that the covered area is five times the area of the aperture, corresponding to 6.9 · FWHM. To remove bright contaminants within the annulus, we apply iterative three sigma clipping. The sigma-clipped median of the annulus is then scaled to the size of the central aperture and subtracted. Afterwards, we correct for flux that is lost outside of the aperture. To do this, we integrate the PSF from equation (1). This yields the fraction of flux within an aperture of radius r,

$$f(r) = 1 - \left[1 + \left(\frac{r^2}{\gamma^2}\right)\right]^{1-\alpha} . \quad (3)$$

This correction is then applied to all measured fluxes. Compared to the noise in the image, the associated error maps seem to be underestimated. This is confirmed by looking at lines with a fixed theoretical ratio, e.g. [O III] λ4958/[O III] λ5007 = 0.35, [O I] λ6363/[O I] λ6300 = 0.33 or [N II] λ6548/[N II] λ6583 = 0.34. By fitting a pair of lines independent from each other and comparing the deviation from the theoretical ratio with the measured uncertainties, we conclude that the uncertainties are underestimated by a factor of 1.38–1.87 (with larger deviations at shorter wavelengths). To compensate for that, we increase the measured uncertainties by a factor of 1.67, reflecting the mean correction factor from our tests. The average uncertainty of the [O III] magnitudes after this correction is 0.078 mag. To this, we add in quadrature the uncertainty that arises from the error of the PSF measurement (estimated to be 0.1 mag on average). This makes up the final value that is reported in Table 2 and used throughout the analysis.

Next, all measured fluxes are corrected for Galactic foreground extinction. For the Milky Way foreground, we use the Cardelli, Clayton & Mathis (1989) extinction curve with $R_V = 3.1$ and $E(B - V)$ from Schlafly & Finkbeiner (2011, see Table 1). We choose not to correct for internal extinction. Neither for circumstellar extinction that is associated with the PN, nor for the dust within the target galaxy. The former is part of the empirical calibration of the luminosity function, and so far only a few studies investigated it (Davis et al. 2018). For the latter, it is common practice not to correct for it, based on a number of arguments (Feldmeier et al. 1997). In the case of the Milky Way, PNe have a higher vertical scale height (Bobylev & Bajkova 2017) than dust (Li et al. 2018). If PNe are equally distributed in front of and behind the dust, we will observe about half of the sample with minimal extinction. As long as this subset sufficiently samples the bright end of the PNLF, we will measure the correct distance. Strictly speaking, this implies that we should observe a different shape, composed of two shifted luminosity functions. In Appendix B we show that our algorithm is able to recover the correct distance even when we have a compound luminosity function, consisting of a sample with extinction and one without extinction. On the other hand, even a few bright PNe that are wrongly extinction corrected can significantly reduce the measured distances.

Finally, the [O III] fluxes (in erg s^{-1} cm^{-2}) are converted to apparent magnitudes with the formula by Jacoby (1989)

$$m_{[\mathrm{O\,III}]} = -2.5 \cdot \log_{10} I_{[\mathrm{O\,III}]} - 13.74 . \quad (4)$$

Table 2. Planetary nebula identifications and supernova remnant contaminants. The full table is available in the online supplementary material.

Galaxy	ID	Type	R.A. (J2000)	Dec. (J2000)	$m_{[\mathrm{O\,III}]}$ mag	$\log(I_{[\mathrm{O\,III}]}/I_{\mathrm{H}\alpha})$	$\log(I_{[\mathrm{N\,II}]}/I_{\mathrm{H}\alpha})$	$\log(I_{[\mathrm{S\,II}]}/I_{\mathrm{H}\alpha})$	Notes
NGC 0628	1	PN	$01^{\mathrm{h}}36^{\mathrm{m}}43\overset{\mathrm{s}}{.}31$	$+15^{\mathrm{d}}47^{\mathrm{m}}18\overset{\mathrm{s}}{.}15$	25.51 ± 0.1	1.1 ± 0.07	−0.83 ± 0.44	−0.71 ± 0.44	
NGC 0628	2	PN	$01^{\mathrm{h}}36^{\mathrm{m}}43\overset{\mathrm{s}}{.}35$	$+15^{\mathrm{d}}47^{\mathrm{m}}18\overset{\mathrm{s}}{.}35$	25.53 ± 0.1	0.67 ± 0.03	−1.24 ± 0.44	−1.13 ± 0.44	
NGC 0628	3	PN	$01^{\mathrm{h}}36^{\mathrm{m}}41\overset{\mathrm{s}}{.}29$	$+15^{\mathrm{d}}47^{\mathrm{m}}04\overset{\mathrm{s}}{.}41$	25.59 ± 0.1	1.75 ± 0.43	−0.03 ± 0.61	0.05 ± 0.61	
NGC 0628	4	PN	$01^{\mathrm{h}}36^{\mathrm{m}}39\overset{\mathrm{s}}{.}96$	$+15^{\mathrm{d}}47^{\mathrm{m}}02\overset{\mathrm{s}}{.}64$	25.59 ± 0.1	0.84 ± 0.04	−1.14 ± 0.44	−1.06 ± 0.44	
NGC 0628	5	PN	$01^{\mathrm{h}}36^{\mathrm{m}}41\overset{\mathrm{s}}{.}37$	$+15^{\mathrm{d}}46^{\mathrm{m}}58\overset{\mathrm{s}}{.}31$	25.66 ± 0.1	0.54 ± 0.03	−1.24 ± 0.44	−1.15 ± 0.44	
NGC 0628	6	PN	$01^{\mathrm{h}}36^{\mathrm{m}}41\overset{\mathrm{s}}{.}37$	$+15^{\mathrm{d}}46^{\mathrm{m}}55\overset{\mathrm{s}}{.}67$	25.67 ± 0.1	1.71 ± 0.43	0.9 ± 0.44	0.06 ± 0.61	
NGC 0628	7	SNR	$01^{\mathrm{h}}36^{\mathrm{m}}42\overset{\mathrm{s}}{.}48$	$+15^{\mathrm{d}}47^{\mathrm{m}}01\overset{\mathrm{s}}{.}48$	25.76 ± 0.1	1.83 ± 0.43	1.58 ± 0.43	1.35 ± 0.43	
NGC 0628	8	PN	$01^{\mathrm{h}}36^{\mathrm{m}}43\overset{\mathrm{s}}{.}35$	$+15^{\mathrm{d}}48^{\mathrm{m}}04\overset{\mathrm{s}}{.}68$	25.85 ± 0.1	0.7 ± 0.04	−1.12 ± 0.44	−0.98 ± 0.44	
NGC 0628	9	PN	$01^{\mathrm{h}}36^{\mathrm{m}}35\overset{\mathrm{s}}{.}82$	$+15^{\mathrm{d}}46^{\mathrm{m}}19\overset{\mathrm{s}}{.}60$	25.94 ± 0.1	0.65 ± 0.03	−0.6 ± 0.09	−1.18 ± 0.44	
NGC 0628	10	PN	$01^{\mathrm{h}}36^{\mathrm{m}}37\overset{\mathrm{s}}{.}95$	$+15^{\mathrm{d}}46^{\mathrm{m}}11\overset{\mathrm{s}}{.}46$	25.97 ± 0.1	0.49 ± 0.02	−0.58 ± 0.06	−0.53 ± 0.07	
⋮	⋮	⋮	⋮	⋮	⋮	⋮	⋮	⋮	⋮
NGC 0628	145	PN	$01^{\mathrm{h}}36^{\mathrm{m}}38\overset{\mathrm{s}}{.}39$	$+15^{\mathrm{d}}48^{\mathrm{m}}24\overset{\mathrm{s}}{.}20$	27.95 ± 0.2	−0.24 ± 0.08	−1.27 ± 0.44	−1.14 ± 0.44	
NGC 0628	146	PN	$01^{\mathrm{h}}36^{\mathrm{m}}36\overset{\mathrm{s}}{.}17$	$+15^{\mathrm{d}}47^{\mathrm{m}}06\overset{\mathrm{s}}{.}59$	27.95 ± 0.19	−0.14 ± 0.07	−1.2 ± 0.44	−1.1 ± 0.44	
NGC 0628	147	PN	$01^{\mathrm{h}}36^{\mathrm{m}}42\overset{\mathrm{s}}{.}34$	$+15^{\mathrm{d}}47^{\mathrm{m}}56\overset{\mathrm{s}}{.}95$	27.95 ± 0.21	0.94 ± 0.44	−0.06 ± 0.61	0.08 ± 0.61	
NGC 0628	148	SNR	$01^{\mathrm{h}}36^{\mathrm{m}}40\overset{\mathrm{s}}{.}53$	$+15^{\mathrm{d}}47^{\mathrm{m}}31\overset{\mathrm{s}}{.}74$	27.97 ± 0.17	0.14 ± 0.07	0.06 ± 0.06	−0.01 ± 0.07	
NGC 0628	149	PN	$01^{\mathrm{h}}36^{\mathrm{m}}42\overset{\mathrm{s}}{.}53$	$+15^{\mathrm{d}}47^{\mathrm{m}}33\overset{\mathrm{s}}{.}41$	27.99 ± 0.21	0.89 ± 0.44	−0.05 ± 0.61	0.06 ± 0.61	

Note. OL: Rejected as overluminous sources.

2.3 Comparison with existing studies

For a handful of galaxies in our sample, the PNLF has been measured in previous studies. This includes NGC 0628 (Herrmann et al. 2008; Kreckel et al. 2017; Roth et al. 2021), NGC 3351 and NGC 3627 (both Ciardullo et al. 2002) and NGC 5068 (Herrmann et al. 2008). To validate our source detection and photometry, we compare the positions and measured fluxes of our PNe candidates when available.

For NGC 0628, we recover around 75 per cent of the sources (including the 20 brightest objects). In Fig. 2, we compare our measured fluxes. While we find good agreement for the [O III] magnitudes, with only minor offsets of $\Delta m_{[\mathrm{O\,III}]} = 0.03 \pm 0.23$ mag (Herrmann et al. 2008), $\Delta m_{[\mathrm{O\,III}]} = 0.01 \pm 0.29$ mag (Kreckel et al. 2017) and $\Delta m_{[\mathrm{O\,III}]} = 0.08 \pm 0.26$ mag (Roth et al. 2021), the Hα fluxes are at odds. Fig. 2 suggests systematically higher Hα fluxes compared to Kreckel et al. (2017). This discrepancy with Kreckel et al. (2017), who used the same data as this work, can be attributed to a different technique for the background subtraction. Kreckel et al. (2017) smoothed the image to 2 arcsec to create a global background map, which is then subtracted from the original image. In our tests, we find that this results in a higher background compared to our annulus background subtraction. The ensuing larger Hα fluxes in our analysis can alter the subsequent classification in favour of H II regions.

For the other galaxies, the overlap is sparse. Narrowband studies have difficulties in removing the stellar continuum and therefore focus on the outer regions to find PNe while our observations do not extend far beyond the central region. Therefore, only a handful of objects appear in both samples. NGC 3351 has six and NGC 3627 has one previously detected PNe in our field of view, and we are able to recover them all. Except for the faintest objects, the [O III] fluxes agree within 0.2 mag, but no Hα fluxes are reported. For NGC 5068, two of their PNe fall in our field of view but we are only able to detect one of them.

2.4 Emission line diagnostics

The galaxies in the PHANGS–MUSE sample are, by selection, star-forming. This means that the detected [O III] emission is not exclusively coming from PNe, but can also originate from H II regions or compact SNRs. To eliminate them from our catalogue of PN candidates, we apply a set of *emission line diagnostics*. The origin of the ionizing radiation is different for the three classes of objects (white dwarfs for PNe, O and B stars for H II regions and shocks for SNRs). This yields different characteristics in their spectra which can be used to discriminate them. The star at the centre of a bright PN is much hotter than the star(s) that ionize an H II region. It has a harder spectrum where more doubly-ionized oxygen is produced compared to Hα (Shaver et al. 1983) and the ratio [O III]/(Hα + [N II]) should therefore be greater than 1.6 (Hα and [N II] are taken together because the lines are close and narrow band imaging can not resolve the individual lines). This effect is even more pronounced for luminous PNe which usually show even higher ratios. Therefore, instead of drawing a straight horizontal line, we use the criterion from Ciardullo et al. (2002) who showed that PNe typically fall above a line defined by

$$\log_{10} \frac{I_{[\mathrm{O\,III}]\,\lambda5007}}{I_{\mathrm{H}\alpha+[\mathrm{N\,II}]\lambda6583}} > -0.37 M_{[\mathrm{O\,III}]} - 1.16\,. \quad (5)$$

This still leaves possible contamination from compact SNRs. To eliminate them, we use a criterion from Blair & Long (2004). The shock-heated material of SNRs will have higher [S II]/Hα ratios with

$$\log_{10} \frac{I_{[\mathrm{S\,II}]\,\lambda6717+[\mathrm{S\,II}]\,\lambda6731}}{I_{\mathrm{H}\alpha}} > -0.4\,. \quad (6)$$

This cut can also remove some H II regions, but it is unlikely that it removes PNe. The classification based on both criteria is shown in Fig. 3. Many of our PN candidates are detected neither in Hα nor in [S II] (we call everything below 3σ undetected). Objects that are consistent within the uncertainty of being a PN are retained in the sample.

A last criterion is given by the velocity dispersion of the emission lines. The shell of a PN expands slowly ($\sim$20 km s^{-1}) into the ambient medium (Schönberner et al. 2005) whereas SNRs have much higher expansion velocities ($\sim$100 km s^{-1}, Franchetti et al. 2012). We measure the velocity dispersion from the [O III] line, averaged over the central pixels of the object, and deconvolve it from the instrumental resolution. We note that, while many objects have quite high signal to noise, the instrumental spectral

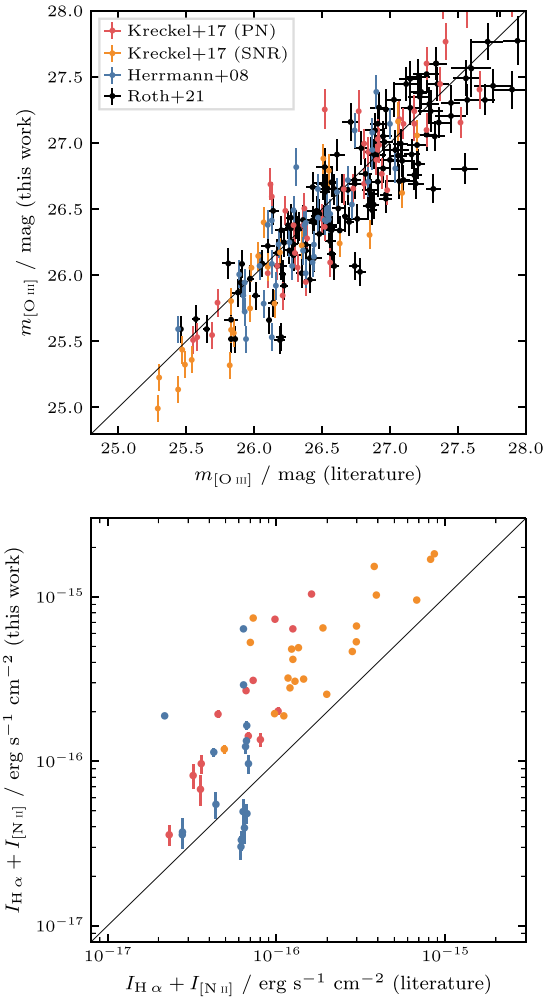

Figure 2. Top panel: Comparison of the [O III] apparent magnitudes in NGC 0628 between our detections and the catalogues from Herrmann et al. (2008), Kreckel et al. (2017) and Roth et al. (2021). The solid line represents equality. Bottom panel: Comparison of the Hα + [N II] fluxes in NGC 0628. Narrowband imaging does not resolve the Hα and [N II] lines individually and instead measures a wider part of the spectrum. While not identical, we try to replicate this behaviour by summing the Hα and the [N II] emission line. The solid line represents equality.

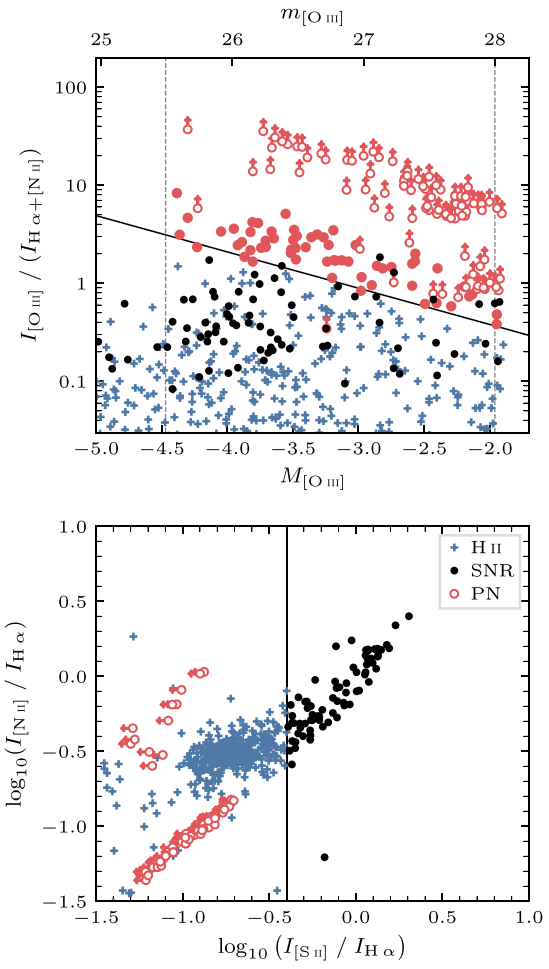

Figure 3. Emission line diagnostics for NGC 0628. The top panel shows the criterion from equation (5) that is used to eliminate H II regions from our sample. Open circles indicate when a PNe is not detected in Hα and the symbol is a lower limit. The lower panel shows the criterion from equation (6) that is used to remove SNRs. Open circles indicate that a PNe is not detected in [S II] and the symbol is an upper limit.

resolution is much larger (∼50 km s^{-1}) than the intrinsic dispersion and so our deconvolution is sensitive to the shape of the assumed line spread function. Because of this, we are confident in relative velocity dispersions, but have reservations about their absolute values. We therefore decide not to use this criterion for the classification, but only as an additional check. Indeed, SNRs (61 km s^{-1}) have a larger velocity dispersion than PNe (48 km s^{-1}) or H II regions (30 km s^{-1}).

2.5 Overluminous sources

The resulting PN catalogue is then visually inspected to exclude any non-point-like objects that slipped through the previous selection process. Most objects that are rejected are removed because their azimuthally averaged radial profile (average flux in annuli of increasing radii, from now on referred to as radial profile) exposes them to be not point-like or they fall very close to another bright object, hampering our ability to measure the flux, but we also have to remove a few objects purely based on their luminosity.

These '*overluminous*' objects are distinctly brighter than the bright end of the remaining luminosity function (see Section 4, Fig. 6), and hence, cannot be described by the PNLF. They have been found in many PN studies (Longobardi et al. 2013; Hartke et al. 2017; Roth et al. 2021), but their exact origin remains unclear (Jacoby, Ciardullo & Harris 1996). Possible explanations include two PNe that accidentally fall close to each other, a misclassified H II region or a background Ly-α galaxy. If such an object falls close to the bright end of the luminosity function, there is no clear way to eliminate it from the sample and it can lead us to underestimate the distances. However, if a gap exists to the remaining sample, it is easy to exclude such an object because the quality of the resulting fit would be very poor. In total, eight objects are rejected as being overluminous. RGB composites of all eight objects are shown in Fig. 4. Three of them are PNe and, therefore, also appear in Fig. 6, while the other five are SNRs that could be classified as PNe.

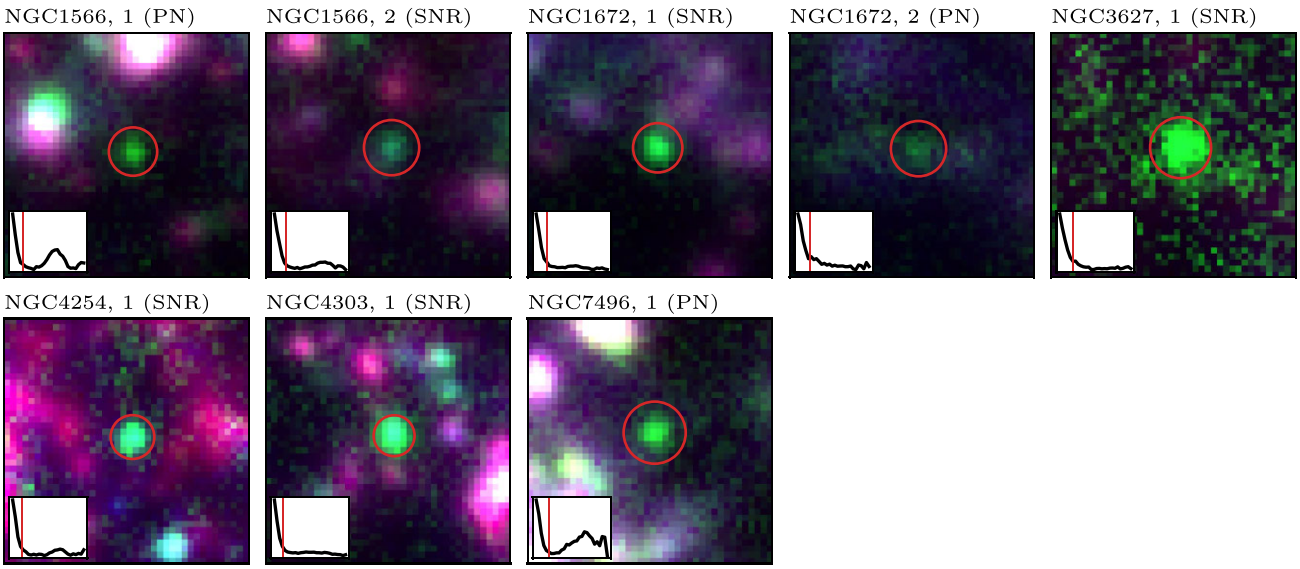

Figure 4. In total eight objects were marked and rejected as overluminous objects. Three of them are PNe and five are SNRs. The cutouts show composite RGB images of those objects with Hα in red, [O III] in green and [S II] in blue. The bottom left corner shows the azimuthally averaged radial profile measured from the [O III] line map. The title contains the name of the galaxy, the 'id' in the catalogue (Table 2) and the type of the object.

2.6 Final PN sample

Based on these detection and selection criteria, we classify 899 objects as PNe across the 19 PHANGS–MUSE galaxies. A further 150 objects are classified as SNRs, which could contaminate narrowband PNe studies, i.e. they satisfy the criterion from equation (5) but not the one from equation (6). The final catalogue is presented in Table 2. The table contains the PNe that are brighter than the completeness limit, and are used in our fit to the PNLF. The position is reported, together with the apparent [O III] magnitude and the line ratios used to make the classification. We also tabulate the SNRs that would be classified as PNe without the [S II] criterion. Special objects like overluminous PNe are flagged with 'OL'.

3 THE PLANETARY NEBULA LUMINOSITY FUNCTION

The *planetary nebula luminosity function* is an empirical relation that describes the number of PNe that we expect to observe at a certain luminosity. Ciardullo et al. (1989a) combined an exponential function from theoretical evolutionary models with a cut-off at the bright end for the following formula:

$$N(M_{[\mathrm{O\,III}]}) \propto \mathrm{e}^{0.307\,M_{[\mathrm{O\,III}]}} \left(1 - \mathrm{e}^{3(M^* - M_{[\mathrm{O\,III}]})}\right) , \quad (7)$$

where M^* is the zero-point of the luminosity function. This simple form of the luminosity function has prevailed even though other parametrizations have been proposed. Hartke et al. (2017), for example, treated the slope of the faint end (0.307 in the original model) as a free parameter and it is even possible to construct a completely numerical luminosity function (e.g. Méndez et al. 2001; Teodorescu et al. 2011).

The zero-point of the luminosity function, M^*, determined by the luminosity of the brightest PN, has more weight in determining the distance than the functional form itself. This value has to be calibrated from PNe in galaxies with known distances. The original value of $M^* = -4.48$ mag was derived based on the Cepheid distance to M 31 by Ciardullo et al. (1989a). A later study by Ciardullo et al. (2002) used galaxies with distances from the *HST* Key Project (Freedman et al. 2001) to quantify the impact of metallicity on the zero-point. They found a modest dependence with an increase at lower metallicities. The metallicity of the galaxies in our sample varies from $12 + \log(\mathrm{O/H}) = 8.41$ to 8.63 in the centre and $12 + \log(\mathrm{O/H}) = 8.00$ to 8.62 at r_{25} (Kreckel et al. 2019; Santoro et al. 2022). Since the expected change in M^* is rather small, we decide to adopt a constant value of $M^* = -4.47$ mag as a starting point. In Section 5.2, we use our measured distances and compare them to existing distances from the tip of the red giant branch (TRGB) to review this relation.

3.1 Completeness limit

Before we fit our data to the luminosity function, we need to estimate the completeness of our sample. Due to noise in the [O III] image and blending with the background, we will miss some of the fainter objects and hence, our luminosity function will not be fully sampled at lower luminosities. To estimate the luminosity where this becomes problematic, we inject mock sources, sampled from a theoretical luminosity function, into the [O III] map and record how many we are able to recover. We never recover 100 per cent because the mock sources are randomly placed in the image and sometimes fall on to crowded areas where they are not detectable. Fig. 5 shows the fraction of recovered objects as a function of their [O III] magnitude.

One could use this function and 'multiply' it with the luminosity function to account for the sources that were missed. Instead, we use an easier approach and fit only the subset of objects that are brighter than a certain threshold. We find that for most galaxies we are able to recover at least 80 per cent of the objects brighter than a limiting magnitude of 28 mag. Including or excluding a few objects at the faint end does not alter the measured distance and we therefore adopt a uniform completeness limit of $m_{[\mathrm{O\,III}]} = 28$ mag. There are two exceptions, NGC 2835 and

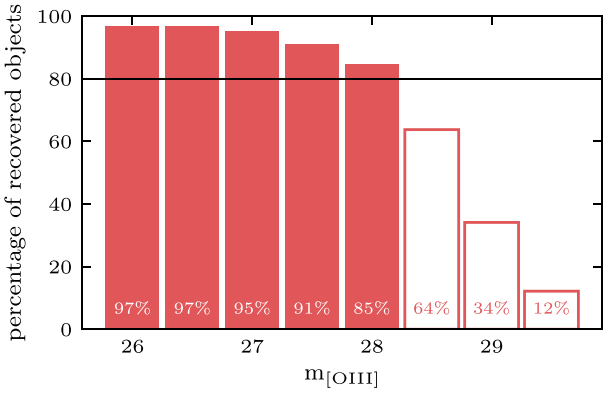

Figure 5. Determining the completeness limit for NGC 0628. We assume our sample to be complete when at least 80 per cent of the sources are recovered ($m_{[\mathrm{O\,III}]} = 28$ mag in this case).

NGC 3627. For these two galaxies, the 80 per cent completeness required by us is only recovered for magnitudes brighter than $m_{[\mathrm{O\,III}]} = 27.5$ mag.

3.2 Fitting the data

We can write the absolute magnitude in terms of the observed apparent magnitude and the distance modulus $\mu = (m - M)$ and fit equation (7) to our observed data. We normalize the function to the number of observed PNe from the root ($=M^* + \mu$) up to the previously determined completeness limit. The fitting itself is done via the method of *maximum likelihood estimation* (MLE; see e.g. Hogg, Bovy & Lang 2010, for a detailed introduction). This alleviates the uncertainties that are introduced when binning the data for a least χ^2 fit. For the MLE, we define the likelihood of a parameter, given some data, as the product of the individual probabilities (or in this case the sum of the log likelihood)

$$\mathcal{L}(\mu) = \sum_i \log p(m_i|\mu)\,. \tag{8}$$

The maximum of this function yields the parameters that best describe our observed data. To account for uncertainties in the observed magnitudes, we calculate the probability of observing a PNe of apparent magnitude $m_{[\mathrm{O\,III}]}$ as the integral of the luminosity function multiplied by a Gaussian centred around the magnitude of the PN with the uncertainty of the apparent magnitude σ_m as the width

$$p(m_{[\mathrm{O\,III}]}) = \int N(m') \frac{1}{\sqrt{2\pi}\sigma_m} \exp\left[-\frac{(m' - m_{[\mathrm{O\,III}]})^2}{2\sigma_m^2}\right] \mathrm{d}m'\,. \tag{9}$$

Strictly speaking, the uncertainties of the magnitudes are not Gaussian (assuming that the uncertainties of the fluxes are). However for sufficiently high signal to noise (>10), the distribution approaches a normal distribution, which is the case for most of our objects. The effect of this procedure is only marginal, but it can take away some weight from the brightest PNe that usually dominate the outcome of the fit. The uncertainty of the fit is taken from the 68 per cent confidence interval of the likelihood function. In Appendix C we look in more detail at the fitting procedure and the reliability of the PNLF.

The classification criterion in equation (5) depends on a prior estimate of the distance, for which we use the distances from Table 1 (Anand et al. 2021) as a starting point. If our measured distance deviates significantly from this value, the classification of some objects might change. To account for this, we use an iterative process where we classify and fit repeatedly until the classification and the measured distance does not change anymore.

Table 3. Measured PNLF distances. N_{PN} is the number of detected PNe brighter than our completeness limit and N_{SNR} is the number of SNRs that could be misclassified as PNe. $(m - M)$ and $(m - M)_{\mathrm{SNR}}$ are the distance moduli measured without and with SNR contamination, respectively.

Name	N_{PN}	N_{SNR}	$(m-M)$ mag	$(m-M)_{\mathrm{SNR}}$ mag	Distance Mpc
IC 5332	47	16	$29.73^{+0.10}_{-0.20}$	$29.78^{+0.09}_{-0.16}$	$8.84^{+0.39}_{-0.82}$
NGC 0628	139	10	$29.89^{+0.06}_{-0.09}$	$29.90^{+0.06}_{-0.09}$	$9.52^{+0.26}_{-0.41}$
NGC 1087	15	5	$31.05^{+0.10}_{-0.24}$	$31.06^{+0.09}_{-0.20}$	$16.25^{+0.74}_{-1.79}$
NGC 1300	17	3	$32.06^{+0.08}_{-0.12}$	$32.03^{+0.07}_{-0.11}$	$25.77^{+0.90}_{-1.42}$
NGC 1365	29	5	$31.22^{+0.08}_{-0.14}$	$31.19^{+0.07}_{-0.13}$	$17.53^{+0.66}_{-1.16}$
NGC 1385	11	9	$29.96^{+0.14}_{-0.32}$	$30.04^{+0.12}_{-0.28}$	$9.81^{+0.63}_{-1.46}$
NGC 1433	90	6	$31.39^{+0.04}_{-0.07}$	$31.39^{+0.04}_{-0.06}$	$18.94^{+0.39}_{-0.56}$
NGC 1512	43	5	$31.27^{+0.07}_{-0.11}$	$31.29^{+0.06}_{-0.10}$	$17.93^{+0.53}_{-0.88}$
NGC 1566	27	2	$31.13^{+0.08}_{-0.17}$	$31.14^{+0.08}_{-0.16}$	$16.84^{+0.60}_{-1.29}$
NGC 1672	19	2	$30.99^{+0.09}_{-0.23}$	$30.98^{+0.09}_{-0.22}$	$15.80^{+0.68}_{-1.68}$
NGC 2835	27	1	$30.57^{+0.08}_{-0.17}$	$30.57^{+0.08}_{-0.17}$	$13.03^{+0.46}_{-1.04}$
NGC 3351	142	10	$30.36^{+0.06}_{-0.08}$	$30.32^{+0.06}_{-0.08}$	$11.80^{+0.31}_{-0.43}$
NGC 3627	43	7	$30.18^{+0.08}_{-0.15}$	$30.16^{+0.07}_{-0.14}$	$10.88^{+0.39}_{-0.77}$
NGC 4254	42	22	$29.97^{+0.09}_{-0.20}$	$29.91^{+0.08}_{-0.16}$	$9.86^{+0.42}_{-0.91}$
NGC 4303	19	7	$30.65^{+0.10}_{-0.26}$	$30.17^{+0.10}_{-0.25}$	$13.49^{+0.64}_{-1.60}$
NGC 4321	62	11	$31.10^{+0.06}_{-0.10}$	$30.78^{+0.08}_{-0.11}$	$16.62^{+0.46}_{-0.74}$
NGC 4535	53	0	$31.43^{+0.06}_{-0.09}$	$31.43^{+0.06}_{-0.09}$	$19.29^{+0.56}_{-0.82}$
NGC 5068	58	22	$28.46^{+0.11}_{-0.26}$	$28.54^{+0.09}_{-0.21}$	$4.93^{+0.24}_{-0.59}$
NGC 7496	13	2	$31.64^{+0.09}_{-0.19}$	$31.04^{+0.11}_{-0.23}$	$21.31^{+0.89}_{-1.89}$

4 RESULTS

In this section, we present an overview of the measured distances and discuss the quality of the individual fits. For each galaxy, we first fit the PNLF to the clean PNe sample and adopt this value as our preferred distance. We then also measure the distance from the catalogue with the potential SNR contaminants to quantify how misclassified SNRs would impact the result. Both values are presented in Table 3. Fig. 6 shows the PNLF for all galaxies in our sample and Fig. 7 shows their cumulative luminosity function. We use a *Kolmogorov–Smirnov test* to compare the observed sample to a theoretical luminosity function. A high test statistic, D_{max} (the maximum distance between the empirical distribution function and the cumulative distribution function of the underlying model), and a low p-value rejects the null hypothesis that the observed data were drawn from the theoretical distribution. The quality of the PNLFs varies greatly in our sample. While the closer galaxies are well sampled, the quality of the fit deteriorates with distance. Beyond 15 Mpc, it becomes increasingly difficult to detect a sufficient number of PNe. This corresponds to a distance modulus of $(m - M) = 30.9$ mag, which puts the bright end cut-off at $m_{[\mathrm{O\,III}]} = 26.4$ mag. With a completeness limit of 28 mag, this means we are only able to observe the upper 1.6 mag of the luminosity function. The reported values for those galaxies should therefore be treated with caution. Fig. 8 shows a comparison between our measured distances with a compilation of literature distance for NGC 0628. Similar plots for the full sample are shown in Appendix A.

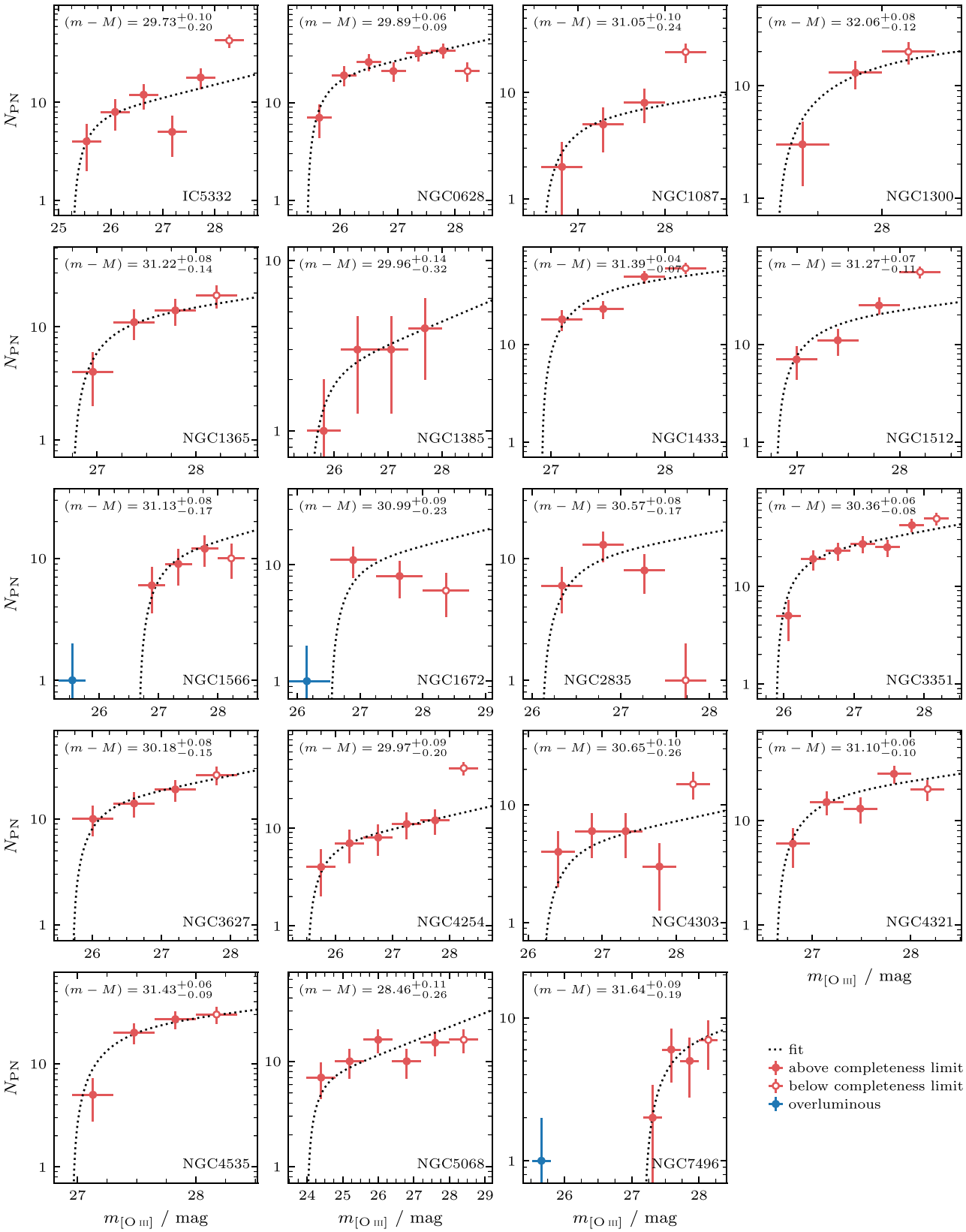

Figure 6. PNLF for all 19 galaxies in our sample. The filled circles denote objects brighter than our completeness limit that contribute to the fit. The *y*-errors are from Poisson statistics and the *x*-errors are the bin widths. The fit of equation (7) is done via the method of maximum likelihood. This binning is only used to illustrate the result and not used in the fit. In blue are objects that were rejected as overluminous objects.

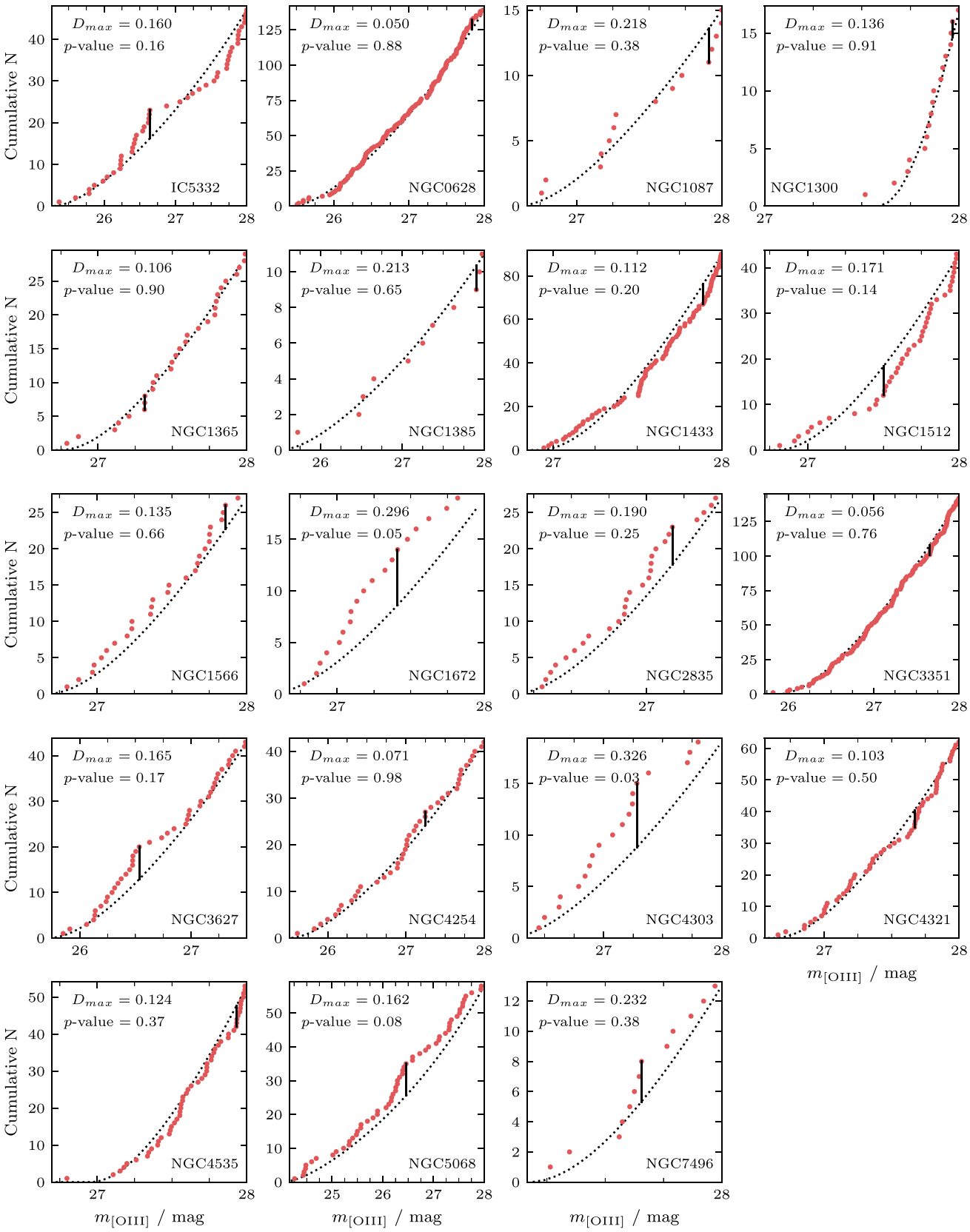

Figure 7. Cumulative PNLF for all 19 galaxies in our sample. In the top left corner is the statistic D_{max} and the p-value from the KS test. The former is indicated with a vertical black bar in the plot (not normalized). The fitted luminosity function is shown with a black dotted line.

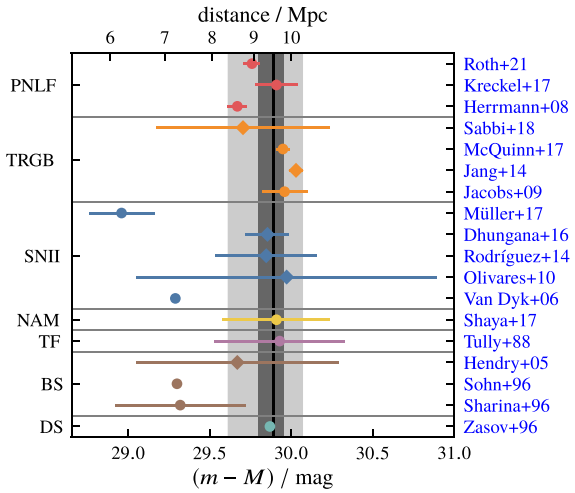

Figure 8. Comparison between our measured distance and literature values for NGC 0628 (M 74). The value measured by this study is marked by a black line with the one and three sigma intervals shaded in grey. We measure a distance modulus of $(m-M) = 29.89^{+0.06}_{-0.09}$ mag ($9.52^{+0.26}_{-0.41}$ Mpc). A list of abbreviations and similar figures for the other galaxies can be found in Appendix A.

IC 5332 is located in the constellation Sculptor. Until recently, the only available distances came from the Tully–Fisher method and they show a large scatter, with the newest reported distance modulus of 29.6 ± 0.4 mag (Tully & Fisher 1988) being significantly larger than the old ones (see Fig. A1). A new TRGB distance from the PHANGS–*HST* program (Anand et al. 2021) finds a distance modulus of 29.77 ± 0.09 mag. This places this galaxy among the closest ones in our sample. Our sample consists of 49 PNe that are brighter than our completeness limit. Two objects were excluded because of their irregular radial profile, but neither of them fall at the bright end, and hence, this does not impact the measured distance. From the remaining 47 PNe we measure a distance modulus of $(m-M) = 29.73^{+0.10}_{-0.20}$ mag ($D = 8.84^{+0.39}_{-0.82}$ Mpc). This is in excellent agreement with the previously mentioned TRGB value and the latest Tully–Fisher distance. There are 16 SNRs that would be classified as PNe without the [S II] line ratio, but none of them fall at the bright end of the luminosity function and their inclusion does not alter the measured distance significantly.

NGC 0628, also known as M 74, is located in the constellation Pisces. This galaxy has been studied extensively with numerous existing distance measurements from different methods (see Fig. 8 for a selection). Among them are the aforementioned PNLF studies by Herrmann et al. (2008), Kreckel et al. (2017) and Roth et al. (2021). This makes this galaxy a valuable benchmark to validate our methods. The distance of Kreckel et al. (2017) is based on the same PHANGS–MUSE data, but was limited to the three pointings that were available at the time, and Roth et al. (2021) uses the same raw data but with a different data reduction. We find 139 PNe that provide a well constrained distance modulus of $(m-M) = 29.89^{+0.06}_{-0.09}$ mag ($D = 9.52^{+0.26}_{-0.41}$ Mpc). This is in excellent agreement to the result from Kreckel et al. (2017) of $(m-M) = 29.91^{+0.08}_{-0.13}$ mag, while both Herrmann et al. (2008) and Roth et al. (2021) derived a smaller distance modulus of $(m-M) = 29.67^{+0.06}_{-0.07}$ mag and $(m-M) = 29.76^{+0.03}_{-0.05}$ mag, respectively. The discrepancy was explained by Kreckel et al. (2017) with SNRs that were misclassified as PNe. We are unable to confirm this explanation. Because we measure larger Hα fluxes (see also Section 2.3), the objects in question are mostly classified as H II regions in our analysis (see Fig. 3) and, therefore, do not factor into the measured distance. Roth et al. (2021) also noted that the brightest PN in their sample is 0.11 mag brighter than the second brightest PN. While not really overluminous, they re-fit their data without this point and obtain a better fit with a larger distance modulus of $(m-M) = 29.87^{+0.03}_{-0.05}$ mag. Taking the catalogue from Roth et al. (2021), we run our fitting algorithm and measure a larger distance modulus of $(m-M) = 29.97^{+0.02}_{-0.05}$ mag (also using the zero-point of $M^* = -4.53$ that they adopted in their paper), indicating that the fitting algorithm and especially the treatment of the uncertainties plays an important role (as Roth et al. (2021) convolved the luminosity function with the photometric error). This galaxy also has a number of TRGB distances (e.g. Jacobs et al. 2009) and they are all in excellent agreement.

NGC 1087 lies in the constellation Cetus. The 15 PNe that are brighter than our completeness limit yield a distance modulus of $(m-M) = 31.05^{+0.10}_{-0.24}$ mag ($D = 16.25^{+0.74}_{-1.79}$ Mpc). This is in agreement with the distances derived from the numerical action method (NAM) or by group affiliation (see Fig. A2).

NGC 1300 is located in the constellation Eridanus and part of the eponymous cluster. Our source detection picks up many extended sources that are associated with very significant Hα emission. Even though this galaxy does not have an active nucleus, we mask the central region and spiral arms to get rid of those objects. We measure a distance modulus of $(m-M) = 32.06^{+0.08}_{-0.12}$ mag ($D = 25.77^{+0.90}_{-1.42}$ Mpc). Our value is considerably larger than the existing literature values (see Fig. A3). However the small sample size of only 17 PNe means that this value is more of an upper limit.

NGC 1365 is also known as the *Great Barred Spiral Galaxy* and is part of the Fornax cluster. This galaxy has an active nucleus and many of the detected objects do not have a clean radial profile, but are instead dominated by noise. From 29 PNe we derive a distance modulus of $(m-M) = 31.22^{+0.08}_{-0.14}$ mag ($D = 17.53^{+0.66}_{-1.16}$ Mpc). This galaxy also has a number of other reliable distance estimates (Fig. A4). Both the two most recent Cepheid distances and the TRGB distance agree well with our measured distance, while another TRGB and Cepheid distance indicate a larger distance.

NGC 1385 we only detect 11 PNe that are brighter than our completeness limit. Most of them are not isolated and have other [O III] emitting sources nearby, which makes the background subtraction more challenging. The derived distance modulus of $(m-M) = 29.96^{+0.14}_{-0.32}$ mag ($D = 9.81^{+0.63}_{-1.46}$ Mpc) is therefore subject to a large uncertainty and should be considered an upper limit for the distance. The value is in good agreement with existing Tully–Fisher distances but shows a large discrepancy to the distance derived with the numerical action method (see Fig. A5). 9 SNRs are potentially misclassified as PNe. None of them fall at the bright end and their inclusion has the opposite effect of increasing the measured distance by 0.08 mag.

NGC 1433 also known as *Miltron's Galaxy*, is a barred spiral galaxy with an active nucleus. We detect 90 PNe that are all isolated with regular radial profile. This is a bit surprising, as the resulting distance modulus of $(m-M) = 31.39^{+0.04}_{-0.07}$ mag ($D = 18.94^{+0.39}_{-0.56}$ Mpc) places it at the far end of our sample where we usually do not find a clean sample. Our measured distance is also significantly larger than all existing literature distances, including a TRGB distance that was measured from LEGUS–*HST* data (Sabbi et al. 2018). We downloaded and reduced the same set of *HST* data, using the technique outlined in Anand et al. (2021), however we are unable to derive a distance based on the colour-magnitude diagram we obtain. The data are relatively shallow and a

possible explanation for the discrepancy is that Sabbi et al. (2018) measured the tip of the AGB and not the tip of the red giant branch.

NGC 1512 is a barred spiral galaxy that is interacting with the nearby galaxy NGC 1510. We find 43 PNe, from which we measure $(m-M) = 31.27^{+0.07}_{-0.11}$ mag ($D = 17.93^{+0.53}_{-0.88}$ Mpc). Similar to NGC 1433, our derived distance is considerably larger than all existing literature distances (see Fig. A7), including again the TRGB distance from LEGUS–*HST* (Sabbi et al. 2018).

NGC 1566 is located in the constellation Dorado. We identify 28 PNe, but one of them is visibly separated from the rest of the luminosity function (by 1 mag) and including it results in a very poor fit. We therefore mark the brightest PN as overluminous and redo the analysis and get a much better fit ($D_{\max} = 0.135$, p-value = 0.66) with a distance modulus of $(m-M) = 31.13^{+0.08}_{-0.17}$ mag ($D = 16.84^{+0.60}_{-1.29}$ Mpc). This is considerably smaller than existing literature values based on the group affiliation (Kourkchi & Tully 2017, see Fig. A8). Five SNRs could be misclassifed as PNe. The brightest among them is as bright as the overluminous PN and is therefore also excluded. The four remaining SNRs do not alter the measured distance.

NGC 1672 is a barred spiral galaxy with an active nucleus (Seyfert type 2). There are two objects that are significantly brighter than the rest (one PN and one SNR). Even when we exclude them, the resulting fit is still rather poor with $D_{\max} = 0.296$, p-value = 0.05 and yields a distance modulus of $(m-M) = 30.99^{+0.09}_{-0.23}$ mag ($D = 15.80^{+0.68}_{-1.68}$ Mpc). The measured value falls between the values derived from the NAM and those derived with Tully–Fisher measurements (see Fig. A9). SNRs do not impact the measured distance.

NGC 2835 this is one of two galaxies where our completeness limit estimation yields a smaller value of 27 mag. However, we do not see a drop in the luminosity function until 27.5 mag (see Fig. 6) and, since the number of detected PNe is already small, we decided to include objects up to 27.5 mag in our sample. From the 27 PNe that match this criterion, we measure a distance modulus of $(m-M) = 30.57^{+0.08}_{-0.17}$ mag ($D = 13.03^{+0.46}_{-1.04}$ Mpc) (we also measure 30.56 mag from the sample with the smaller completeness limit). Existing Tully–Fisher distances arrive at a smaller distance, but a recent TRGB distance from Anand et al. (2021) is in good agreement with our value (see Fig. A10).

NGC 3351 also known as M 95, is a barred spiral galaxy located in the Leo constellation that has a characteristic ring. This is one of the few galaxies in our sample with an existing PNLF distance. Ciardullo et al. (2002) measured a distance modulus of $(m-M) = 30.05^{+0.08}_{-0.16}$. We recover the six PNe that fall in our field of view, however two of them are classified differently. We classify their 5$^{\text{th}}$ brightest PN as a SNR and their 6$^{\text{th}}$ brightest object is classified as an H II region. This galaxy has the second largest number of PN detections in our sample and we find an excellent fit with a distance modulus of $(m-M) = 30.36^{+0.06}_{-0.08}$ mag ($D = 11.80^{+0.31}_{-0.43}$ Mpc). This is significantly larger than the previous PNLF distance and also larger than most of the existing TRGB (e.g. Rizzi et al. 2007; Sabbi et al. 2018) and Cepheid (e.g. Freedman et al. 2001; Saha et al. 2006) distances. There are however also a TRGB distance (Sakai et al. 2004) that is in good agreement and a Cepheid distance (Paturel & Teerikorpi 2006) that is even larger (see Fig. A11).

NGC 3627 also known as M 66, can also be found in the constellation Leo and is part of the Leo Triplet. This is the second galaxy from Ciardullo et al. (2002) that is also in our sample, but only one of the PNe that was detected in that paper falls within our field of view. We recover this object and measure the same $m_{[\text{O III}]}$ magnitude but classify it as a SNR. This object is the 35$^{\text{th}}$ brightest PN in the catalogue of Ciardullo et al. (2002). Therefore, this misclassification will hardly impact the result. Their brighter PNe all fall outside of our field of view and, hence, we can not make any statements about them. In our PN sample, this object would constitute one of the brightest object. Including this object would have a minuscule effect on our result and decrease the measured distance modulus by 0.02 mag. The distance modulus that we measure from the clean PNe sample is $(m-M) = 30.18^{+0.08}_{-0.15}$ mag ($D = 10.88^{+0.39}_{-0.77}$ Mpc). This is in good agreement with the existing PNLF distance of $(m-M) = 29.99^{+0.07}_{-0.08}$ or other recent TRGB distances (e.g. Anand et al. 2021; Jacobs et al. 2009, see Fig. A12). There are 8 potential SNR contaminants, one of which is overluminous. If we exclude this object, the measured distance is not impacted by the other 7 SNRs.

NGC 4254 also known as M 99, is one of four galaxies in our sample that are part of the Virgo cluster. 45 objects constitute our initial PNe catalogue. However, a large number of objects are surrounded by strong Hα emission and three objects are rejected because of their irregular radial profile. Despite this, the remaining 42 PNe provided an excellent fit with $D_{\max} = 0.071$, p-value = 0.982 and yield a distance modulus of $(m-M) = 29.97^{+0.09}_{-0.20}$ mag ($D = 9.86^{+0.42}_{-0.91}$ Mpc). This is smaller than all previously published distances. Among them are two distances based on the type II supernova SN1986I (Nugent et al. 2006; Poznanski et al. 2009) and a number of Tully–Fisher estimates. They all indicate a larger distance modulus around $(m-M) = 30.75$ mag (see Fig. A13). The Hubble velocity of this galaxy is 2400 km s^{-1} (Springob et al. 2005) and also implies a significant larger distance. The inclusion of 22 misclassified SNRs does not affect the measured distance (one SNR is removed because it is clearly overluminous).

NGC 4303 also known as M 61, is also part of the Virgo Cluster and an active (Seyfert type 2) barred spiral galaxy. We detect 19 PNe from which we measure $(m-M) = 30.65^{+0.10}_{-0.26}$ mag ($D =$ Mpc), but the fit is not good with $D_{\max} = 0.326$, p-value = 0.03. This galaxy did not have a good distance estimate, only a number of type II supernovae that do not agree on one distance as well as some uncertain Tully–Fisher estimates. Eight SNR could be misclassified as PNe. One of them is clearly overluminous (1.2 mag below the next three objects and 1.8 mag below the rest). The next three brightest objects are also SNRs and they are 0.6 mag brighter than the bright end of the PNLF. While there is a gap in the luminosity function, their inclusion improves the fit ($D_{\max} = 0.243$, p-value = 0.227) and they are therefore retained in the sample. With them, the measured distance is decreased by 0.48 mag.

NGC 4321 also known as M 100 is located in the Virgo cluster. It is a low ionization nuclear emission region (LINER) galaxy and we mask out the centre and the spiral arms. We get a decent fit ($D_{\max} = 0.103$, p-value = 0.50) and measure a distance modulus of $(m-M) = 31.10^{+0.06}_{-0.10}$ mag ($D = 16.62^{+0.46}_{-0.74}$ Mpc) from 62 PNe. NGC 4321 has existing literature distances from Cepheids (Freedman et al. 2001; Tammann, Sandage & Reindl 2008) and a recent TRGB distance from Anand et al. (2021). They all agree with our reported value. Out of 11 SNRs, one falls 0.6 mag below the bright end cut-off. With this object, the measured distance modulus decreases to $30.78^{+0.08}_{-0.11}$ mag. If we only include the other 10 SNRs, the distance modulus is very similar to the one derived from the clean PN sample ($31.053^{+0.06}_{-0.09}$ mag). However the fit is not bad enough ($D_{\max} = 0.108$, p-value = 0.336), to exclude this one object as overluminous.

NGC 4535 is the fourth galaxy in our sample that is part of the Virgo Cluster. From 53 PN we measure $(m-M) = 31.43^{+0.06}_{-0.09}$ mag ($19.29^{+0.56}_{-0.82}$ Mpc). This is in good agreement to the Cepheid distance from Paturel & Teerikorpi (2006) who reported a value of 31.6 mag, but significantly bigger than other Cepheid distances (e.g. Freedman

et al. 2001, 30.85 + −0.05 mag). This is the only galaxy for which we do not find any potentially misclassified SNRs.

Noteworthy is the large range of distances that we obtained for the four Virgo galaxies in our sample (ranging from 9.86 Mpc for NGC 4254 to 19.29 Mpc for NGC 4535). Among all galaxies in the cluster, there are a few published distances that are smaller than our value for NGC 4254, but neither of them is coming from TRGB, Cepheid or PNLF measurements.

NGC 5068 is located in the Virgo constellation. This is the nearest and also the least massive galaxy in our sample. We find 58 PNe and our fit yields a distance modulus of $(m - M) = 28.46^{+0.11}_{-0.26}$ mag ($4.93^{+0.24}_{-0.59}$ Mpc). This is another galaxies with an existing PNLF distance from Herrmann et al. (2008). Unfortunately, only two of their PN are in the central region that is covered by our observations. We only recover one of them and the [O III] line map does not show any emission at the location of the second one. The data from Herrmann et al. (2008) indicate a larger distance of $28.85^{+0.09}_{-0.16}$ mag. Because of the lower metallicity of this galaxy, they decide to use a fainter M^* and obtain the reported distance of $(m - M) = 28.68^{+0.08}_{-0.18}$. We do not apply such a correction here, as this would even further decrease our measured distance, which is already smaller than the existing PNLF and TRGB distances. Within the uncertainties, our distance is in good agreement to the TRGB distances from Anand et al. (2021) and Karachentsev et al. (2017). While there is a large number of SNRs (22), their inclusion does not alter the measured distance.

NGC 7496 is a barred spiral galaxy with Seyfert type 2 activity, located in the constellation Grus. PHANGS–MUSE covered these galaxies with only three pointings. Due to the active core, we mask the central part and arms, leading to the detection of only 14 PNe and 2 SNRs that could be misclassified. One PNe was excluded as an overluminous object. Previous distance estimates were all based on the Tully–Fisher method, with a large scatter between the different studies. Our distance modulus of $(m - M) = 31.64^{+0.09}_{-0.19}$ mag ($4.93^{+0.24}_{-0.59}$ Mpc) is in good agreement to NAM distance modulus of $(m - M) = 31.36 \pm 0.33$ mag. Both of the SNRs fall slightly below the bright and decreases the measured distance by 0.60 mag. The few data points that we have for this galaxy makes it difficult to judge whether these two points belong to the sample or not.

5 DISCUSSION

5.1 Comparison with literature distances

To benchmark our results, we compare them to published distances. We have literature distances for all galaxies, for some galaxies from a myriad of different methods (see Appendix A). For the four galaxies with existing PNLF distances, we find excellent agreement with less than 1σ difference for NGC 0628 (derived from the same data) and NGC 3627, while the previous PNLF distance to NGC 5068 is slightly larger (2σ) and the previous PNLF distance to NGC 3351 is significantly smaller (3.8σ).

Ten galaxies also have TRGB distances and with the exception of NGC 1433 and NGC 1512, they are in good agreement with our values. Furthermore, we have five galaxies with Cepheid distance. The distances derived with this method often vary between studies and our results always fall within the range of published distances. PNLF distances have historically shown a systematic offset to distances measured from surface brightness fluctuations (SBF) (Ciardullo et al. 2002). However, as there are no elliptical galaxies in the PHANGS sample, we have no SBF distances to compare with. To check for systematic offsets between our PNLF distances and other methods, we plot the difference $\Delta(m - M) = (m - M)_{\rm ref} - (m - M)_{\rm PHANGS}$ between a number of commonly used distance indicators and our derived distance modulus in Fig. 9. The plot shows generally good agreement between the different methods, but there is a slight systematic offset as our PNLF distances are on average larger than the literature distances across all methods. However the offsets are generally small and always smaller than the scatter. The rather large scatter compared to the literature TRGB distances mostly stems from the discrepancies with the distances to NGC 1433 and NGC 1512. In Section 4 we provided a possible explanation for this and if we exclude them from the comparison, the TRGB method shows an excellent agreement with $\Delta(m - M) = -0.04 \pm 0.18$ mag.

The galaxies that previously lacked a good distance estimate (i.e. from the PNLF, TRGB or Cepheids) are NGC 1087, NGC 1300, NGC 1385, NGC 1672, NGC 4254, NGC 4303 and NGC 7496. Unfortunately, these are also the galaxies with the fewest PN detections, which in general leads to larger errors on the measured distances. However they are usually still smaller than what is available in the literature.

5.2 Zero point of the PNLF

The single most important input to the PNLF is the zero-point. For our analysis, we assume a constant value across all galaxies, but theoretical models (Dopita, Jacoby & Vassiliadis 1992) and observations (Ciardullo et al. 2002) indicate an increase of M^* at low metallicities. The change can be described by a quadratic formula,[2]

$$\Delta M^* = 0.928\,[\mathrm{O/H}]^2 - 0.109\,[\mathrm{O/H}] + 0.004\,, \quad (10)$$

with the solar oxygen abundance $12 + \log(\mathrm{O/H})_\odot = 8.69$ from Asplund et al. (2009). We can compare our measured distances to literature distances to re-examine this relation. For this, we use the distances in Table 1 that were curated by Anand et al. (2021). We only use the subsample that is based on the TRGB (8 galaxies). To first approximation the change in the zero-point is given by $\Delta M^* \approx (m - M)_{\rm PNLF} - (m - M)_{\rm ref}$. We use this as a starting point in our PNLF fit and vary M^* until we reproduce the literature distance.

One distinct advantage of IFU observations is that one can derive the PNLF distance and the metallicity from the same data. For our data, the gas-phase oxygen abundance is measured from H II regions (based on the S-calibration from Pilyugin & Grebel 2016) by Kreckel et al. (2019) and Santoro et al. (2022). We use their linear abundance gradient fits to calculate the metallicity at the mean radius of the PNe (see Table 1). In contrast, the metallicities that were used in Ciardullo et al. (2002) were compiled by Ferrarese et al. (2000a) from different literature sources (most of them are based on the strong line method calibration by Dopita & Evans 1986). The galaxies that overlap with our sample (NGC 3351 and NGC 3627) show a large discrepancy of ∼0.7 dex between the PHANGS and literature metallicity (considerably more than what could be explained by differences in the value for the solar oxygen abundance). More recent abundances from Pilyugin, Grebel & Kniazev (2014) and Toribio San Cipriano et al. (2017) (for the SMC and LMC) show much better agreement with our sample (see top panel of Fig. 10). This result shows that such analysis is severely hampered by uncertainties in the metallicity prescriptions and greatly benefits from the homogeneous sample that IFU observations can provide.

[2] Adopted from Ciardullo et al. (2002) but with $12 + \log(\mathrm{O/H})_\odot$ from Asplund et al. (2009) instead of Grevesse, Noels & Sauval (1996).

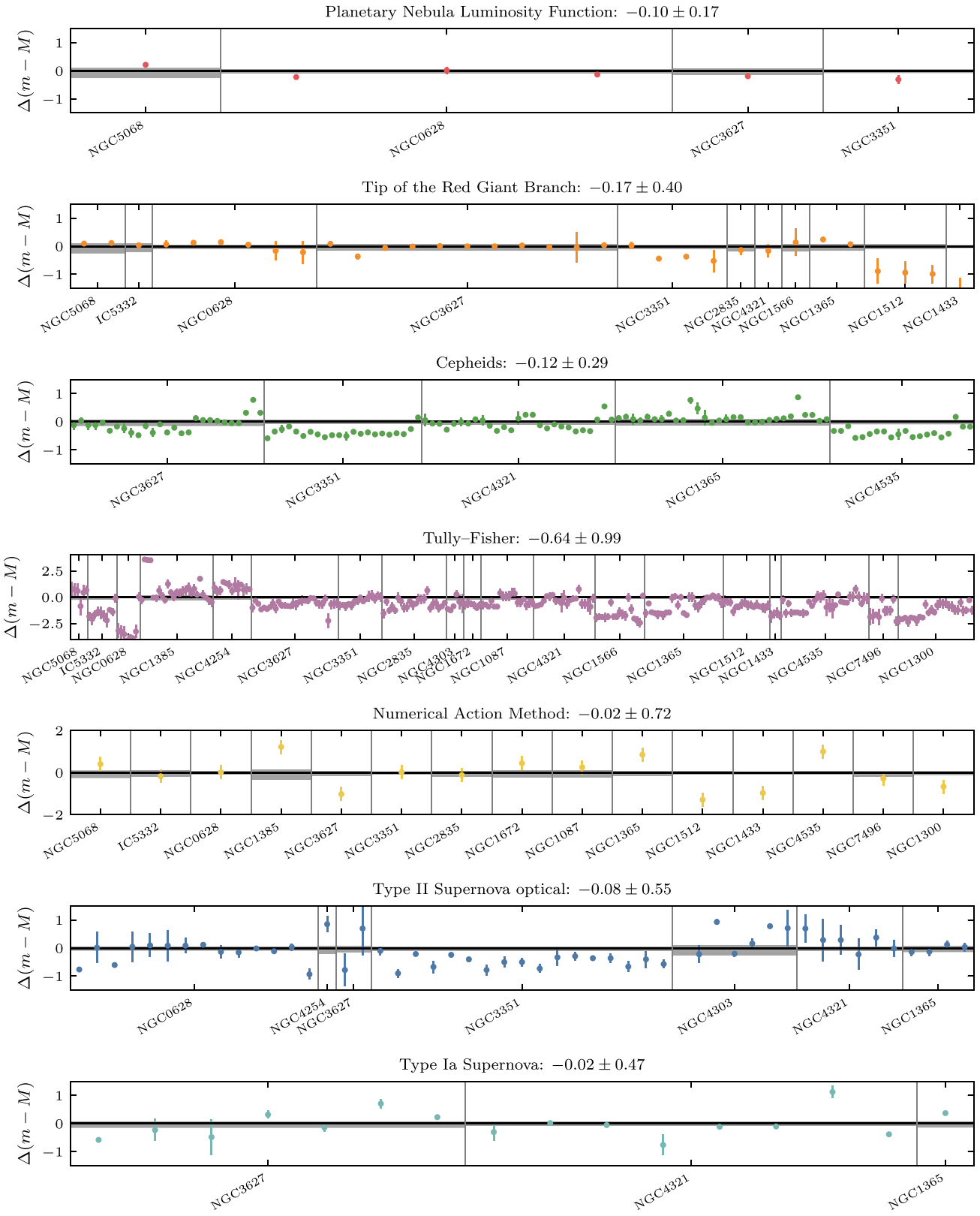

Figure 9. Comparison with literature distances, taken from NED. Shown is the difference between our value and the literature $\Delta(m-M) = (m-M)_{\rm ref} - (m-M)_{\rm PHANGS}$. The galaxies are sorted by distance and the points for each galaxy are sorted by year of publication. If more than one value was published for a source, each value is shown separately. The uncertainties of our measurement is indicated by the grey shaded area.

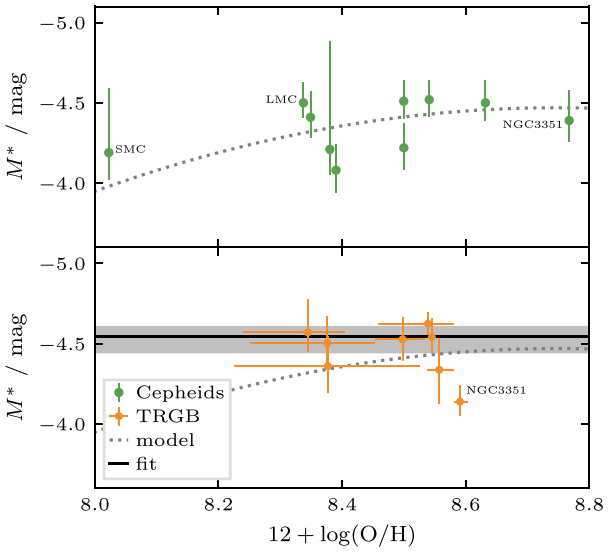

Figure 10. Determining the zero-point of the PNLF. The points in the top panel are based on Cepheid distances from Ciardullo et al. (2002) and abundances from Pilyugin et al. (2014). The points in the lower panel are based on our measured distances in combination with existing TRGB distances from Table 1. The metallicity is determined by taking the value of the H II region metallicity gradient (Kreckel et al. 2019; Santoro et al. 2022) at the mean galactic radius of the PNe. The error bars in x-direction represent the minimum and maximum abundance for the PNe in our sample. The dotted curve shows the theoretical dependence from equation (10) and the solid line is a fit with a constant line (with the 1σ interval in grey). Overall our sample is consistent with a constant zero-point.

Our sample lacks low metallicity galaxies to constrain the decrease at low metallicities and Ciardullo (2012) found that for galaxies with metallicities above the LMC, the zero-point is roughly constant. Even though we can not test the metallicity dependence, it is still worth to re-examine the zero-point. Fitting a constant line to our own data (see lower panel of Fig. 10) we find a zero-point of $-4.469^{+0.049}_{-0.025}$ mag. The fit is heavily skewed by NGC 3351 where our distance is more than 3σ larger than the TRGB distance. We therefore use a mixture model for outlier pruning (Foreman-Mackey 2014) with which we measure a zero-point of $-4.542^{+0.103}_{-0.059}$ mag. This value is in excellent agreement to the value that Ciardullo (2012) derived with the help of TRGB distances. Because our sample only consists of 8 points, one of which is rejected by the outlier pruning, we prefer to use the initial adopted value of $M^* = -4.47$ for the PNLF distances computed in this paper. Given the growing databases of galaxies with both TRGB distances and optical IFU data in the archives, this topic is ripe for future work to revisit this question using larger samples of galaxies.

5.3 Contamination with supernova remnants

Since Kreckel et al. (2017) found that SNRs that are misclassified as PNe can alter the distances measured from the PNLF, the question stood whether narrowband observations are sufficient for PN studies. In order for SNRs to bias the results, they must meet a couple of criteria. First of all, they must be classified as PN by narrowband studies. As we see in Fig. 3, most SNRs are in a regime where they would be classified as H II regions without the additional diagnostics from the [S II] line. Second, the contamination must occur at the bright end of the luminosity function. The way the fitting of the PNLF works, only the brightest objects have a noticeable contribution to the outcome. Third, the contaminant must not be too much brighter than the bright end cut-off. When a single object is much brighter than the main sample, it makes the fit worse and is therefore easily excluded as being overluminous. Hence, either a single SNR close to the bright end or a number of SNRs that are fainter than the bright end are needed to change the distance.

In almost all galaxies in our sample, we find at least one SNR that could be classified as a PN without the [S II] criteria. However, only in the case of three galaxies do the misclassified objects have a significant impact the measured distance. This is the case for NGC 4303 (−0.48 mag), NGC 4321 (−0.33 mag) and NGC 7496 (−0.60 mag). In the case of NGC 4303, three SNRs fall 0.5 mag below the cut-off, however they do not worsen the fit, making it difficult to justify their exclusion. NGC 4321 has one SNR that is clearly separated from the rest of the sample, but the goodness of the fit is not impacted. Finally for NGC 7496 the sample is too small to reliably exclude the two slightly overluminous SNRs.

Directly related to this is the challenge in accurately determining the flux emitted by an object. The largest uncertainty arises from background contamination. The [O III] line fluxes are relatively robust because there is little to no background emission. However, this is not the case for Hα. The background can have a significant contribution and so correct background subtraction is crucial. As shown in Fig. 2, different approaches to the background subtraction can lead to vastly different results for the Hα fluxes. If not done properly, wrong fluxes can alter the line ratios and hence the classification of objects.

5.4 Limitations of IFU observations to the PNLF

The PNLF is rarely applied to galaxies beyond 20 Mpc, since with narrowband imaging, the expected flux from a single PN at larger distances is similar to the background. Recent attempts by Ventimiglia, Arnaboldi & Gerhard (2011), Arnaboldi et al. (2013), or Roth et al. (2021) have pushed the limits of what is possible by using multi-slit imaging spectroscopy or IFU spectroscopy. Here, we make a rough estimate on the maximum distance that can be measured from MUSE with exposure times similar to our observations (43 min). We require a certain number of PN detections (from our experience $\gtrsim$ 20) in order to measure a reliable distance. However, it is difficult to predict the number of PNe that one can expect to observe in a given galaxy, as it depends on a number of parameters. It relies foremost on the underlying stellar population. More stars means more PNe. To compare the number of detected PNe between galaxies, it is useful to define the *luminosity-specific planetary nebula number*,[3]

$$\alpha = \log_{10} \frac{N_{\rm PN}}{L_{\rm bol}} \,, \tag{11}$$

where $N_{\rm PN}$ is the number of detected PNe above our completeness limit and $L_{\rm bol}$ is the bolometric luminosity of the surveyed area. The bolometric luminosity of the survey area is estimated from a simulated V-band image via a bolometric correction. We use $f_\lambda = 363.1 \times 10^{-11}\,{\rm erg\,s^{-1}\,cm^{-2}\,\AA^{-1}}$ (Bessell, Castelli & Plez 1998) as the zero-point to convert fluxes into magnitudes and then calculate the bolometric luminosity as

$$L_{\rm bol} = 10^{-0.4(M_V - 4.79)}\, 10^{-0.4({\rm BC}_V + 0.07)}\, {\rm L}_\odot \,, \tag{12}$$

[3]this definition is different from the $\alpha_{2.5}$ that is common in the literature (e.g. Hartke et al. 2017) in that we only use the number of PNe that are brighter than our completeness limit and not within a fixed range above the bright end cut-off.

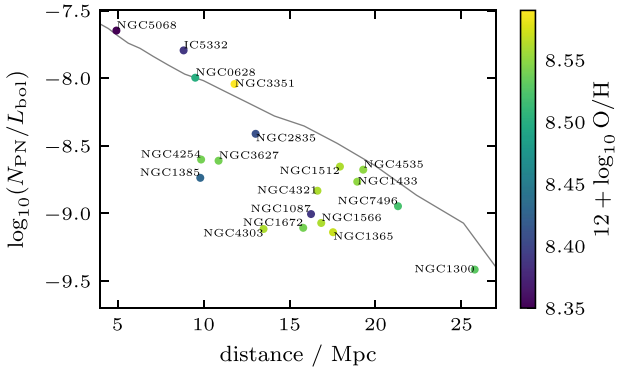

Figure 11. Luminosity-specific planetary nebula number as a function of distance. The number of detections decreases with distance because we sample a smaller range of the PNLF. The grey line uses NGC 0628 as a reference and shows the expected decrease of α based on the sampled part of the PNLF.

with $BC_V = -0.85$ mag (from Buzzoni et al. 2006). Since we also have stellar mass maps, we could also utilize those instead, but due to its prevalence in the literature, we opt to use $L_{\rm bol}$. Both yield similar results.

Because all galaxies have the same observed completeness limit (for NGC 2835 and NGC 3627 we extrapolate the number of PNe to match the other galaxies), the part of the PNLF that we observe decreases with distance. This reduces $N_{\rm PN}$ while $L_{\rm bol}$ remains unaffected and, hence, we expect a decrease in α as can be seen in Fig. 11. As evident in Fig. 11, compared to NGC 0628, more than half of the galaxies in our sample have fewer PNe than expected. We find up to a factor of 7 difference in the number of PNe. A possible explanation is a decrease of α with metallicity. But our galaxies are all similar and only show small variations in metallicity (0.24 dex). The observed change is too large to be explained by the models of Buzzoni et al. (2006). However, a recent study by Galán-de Anta et al. (2021) also finds comparable differences.

We can use this relation to calculate the farthest distance at which we are able to obtain a sufficient number of PNe to measure a reliable distance. For each galaxy, we use the previously measured $L_{\rm bol}$ to calculate the α that corresponds to $N_{\rm PN} = 20$. We can then compute the distance that corresponds to this value based on the sampling of the PNLF. Based on this analysis, we find the largest possible distance that could be measured for a galaxy in our sample is ∼26 Mpc.

To some degree, the number of detections should also decrease with resolution as fainter objects start to blend in with their background at coarser resolution. However, Kreckel et al. (2017) showed that this only becomes an issue above 100 pc physical resolution. With the typical seeing that we achieve with MUSE (0.60 arcsec with AO and 0.76 arcsec without), this corresponds to a distance of 34.38 Mpc and 27.14 Mpc, respectively, both above what we could measure. This means that this issue should only concerns less powerful IFU instruments with a coarser spatial resolution and indeed we do not see any obvious connection between the resolution and the number of detections in our data.

6 CONCLUSIONS

We use VLT/MUSE observations obtained by the PHANGS collaboration to identify 899 PNe across 19 nearby galaxies. We then calculate new PNLF distances for each galaxy (see Table 3), 15 of which did not have a PNLF distance before. This significantly increases the number of galaxies with PNLF distances, which previously stood at around 70. Fourteen galaxies achieve an uncertainty better than 10 per cent and six galaxies better than 5 per cent.

When comparing with other studies, we find good agreement of the [O III] line fluxes but significant variations in the H α line fluxes. This can be traced back to different techniques for background subtraction (unlike [O III], H α has a significant background contribution). This highlights the difficulty of the background subtraction which can have a major impact on the classification and, thereby, ultimately also on the measured distance.

The findings of Kreckel et al. (2017) raised questions about the reliability of narrowband observations for PN studies, with the possibility of misclassified SNRs biasing the measured distance. While we can not reproduce this issue in the particular case of NGC 0628, we find three other galaxies where SNRs can impact the measured distance. For the other galaxies, the changes are insignificant and smaller than the uncertainties. Most misclassified SNRs fall in the regime of H II regions, and hence, do not contribute to the measured distance. The few SNRs that are classified as PNe often are at the faint end of the luminosity function where their contribution is negligible.

With metallicities derived from the same MUSE data and TRGB distances from the literature, we revisit the calibration of the PNLF zero-point. Our sample is consistent with a constant zero-point and we find a value of $-4.542^{+0.103}_{-0.059}$ mag.

Because they do not require dedicated observations, IFU surveys can potentially multiply the number of galaxies with PNLF distances in the near future. A growing number of spectral imaging surveys that utilize VLT/MUSE like MAD (den Brok et al. 2020) or TIMER (Gadotti et al. 2019), or CFHT/SITELLE like SIGNALS (Rousseau-Nepton et al. 2019) fill the archives with a plethora of suitable observations that could be harnessed to measure PNLF distances.

ACKNOWLEDGEMENTS

We thank the anonymous referee for the helpful comments that improved this work. This work was carried out as part of the PHANGS collaboration. Based on observations collected at the European Southern Observatory under ESO programmes 1100.B-0651, 095.C-0473, and 094.C-0623 (PHANGS–MUSE; PI Schinnerer), as well as 094.B-0321 (MAGNUM; PI Marconi), 099.B-0242, 0100.B-0116, 098.B-0551 (MAD; PI Carollo) and 097.B-0640 (TIMER; PI Gadotti). FS and KK gratefully acknowledges funding from the German Research Foundation (DFG) in the form of an Emmy Noether Research Group (grant number KR4598/2-1, PI Kreckel). GA acknowledges support from the IPAC Visiting Graduate Fellowship programme and from an award from the Space Telescope Science Institute in support of programme SNAP-15922. FS, ES and TGW acknowledge funding from the ERC under the European Union's Horizon 2020 research and innovation programme (grant agreement no. 694343). ATB and FB would like to acknowledge funding from the European Research Council (ERC) under the European Union's Horizon 2020 research and innovation programme (grant agreement No. 726384/Empire). SCOG and RSK acknowledge support from the DFG via SFB 881 'The Milky Way System' (project-ID 138713538; subprojects A1, B1, B2, and B8) and from the Heidelberg cluster of excellence EXC 2181-390900948 'STRUCTURES: A unifying approach to emergent phenomena in the physical world, mathematics, and complex data', funded by the German Excellence Strategy. RSK also thanks for support from the European Research Council via the ERC Synergy Grant 'ECOGAL – Understanding our Galactic ecosystem: From the disc of the

Milky Way to the formation sites of stars and planets' (contract number 855130). JMDK gratefully acknowledges funding from the Deutsche Forschungsgemeinschaft (DFG, German Research Foundation) through an Emmy Noether Research Group (grant number KR4801/1-1) and the DFG Sachbeihilfe (grant number KR4801/2-1), as well as from the European Research Council (ERC) under the European Union's Horizon 2020 research and innovation programme via the ERC Starting Grant MUSTANG (grant agreement number 714907). ER acknowledges the support of the Natural Sciences and Engineering Research Council of Canada (NSERC), funding reference number RGPIN-2017-03987. EW acknowledges support from the DFG via SFB 881 'The Milky Way System' (project-ID 138713538; subproject P2).

This research has made use of the NASA/IPAC Extragalactic Database (NED) which is operated by the Jet Propulsion Laboratory, California Institute of Technology, under contract with NASA. It also made use of a number of python packages, namely PHOTUTILS, an Astropy package for detection and photometry of astronomical sources (Bradley et al. 2019) as well as the main ASTROPY package (Astropy Collaboration 2013, 2018), NUMPY (Harris et al. 2020) and MATPLOTLIB (Hunter 2007).

DATA AVAILABILITY

The MUSE data underlying this article are presented in Emsellem et al. (2021) and are available at the ESO archive. The catalogue with the planetary nebulae identifications is available in the online supplementary material of the journal. The code for this project is available at https://github.com/fschmnn/pnlf.

REFERENCES

Amanullah R. et al., 2010, ApJ, 716, 712
Anand G. S. et al., 2021, MNRAS, 501, 3621
Arnaboldi M., Longobardi A., Gerhard O., Okamura S., 2013, in de Grijs R., ed., Proc. IAU Symp. 289, Advancing the Physics of Cosmic Distances. Kluwer, Dordrecht, p. 287
Asplund M., Grevesse N., Sauval A. J., Scott P., 2009, ARA&A, 47, 481
Astropy Collaboration, 2013, A&A, 558, A33
Astropy Collaboration, 2018, AJ, 156, 123
Bacon R. et al., 2010, in Ground-based and Airborne Instrumentation for Astronomy III. p. 773508
Bacon R. et al., 2017, A&A, 608, A1
Baldwin J. A., Phillips M. M., Terlevich R., 1981, PASP, 93, 5
Barbarino C. et al., 2015, MNRAS, 448, 2312
Bartel N., Bietenholz M. F., 2003, ApJ, 591, 301
Bartel N., Rogers A. E. E., Shapiro I. I., Gorenstein M. V., Gwinn C. R., Marcaide J. M., Weiler K. W., 1985, Nature, 318, 25
Belfiore F. et al., 2019, AJ, 158, 160
Bernal J. L., Verde L., Riess A. G., 2016, J. Cosmology Astropart. Phys., 2016, 019
Bessell M. S., Castelli F., Plez B., 1998, A&A, 333, 231
Blair W. P., Long K. S., 2004, ApJS, 155, 101
Bobylev V. V., Bajkova A. T., 2017, Astron. Lett., 43, 304
Bojičić I. S., Filipović M. D., Urošević D., Parker Q. A., Galvin T. J., 2021, MNRAS, 503, 2887
Bose S., Kumar B., 2014, ApJ, 782, 98
Bottinelli L., Gouguenheim L., Paturel G., de Vaucouleurs G., 1984, A&AS, 56, 381
Bottinelli L., Gouguenheim L., Paturel G., de Vaucouleurs G., 1985, A&AS, 59, 43
Bottinelli L., Gouguenheim L., Paturel G., Teerikorpi P., 1986, A&A, 156, 157
Bradley L. et al., 2019, astropy/photutils: v0.6. Zenodo, available at https://doi.org/10.5281/zenodo.2533376
Branch D., Falk S. W., McCall M. L., Rybski P., Uomoto A. K., Wills B. J., 1981, ApJ, 244, 780
Burns C. R. et al., 2011, AJ, 141, 19
Buzzoni A., Arnaboldi M., Corradi R. L. M., 2006, MNRAS, 368, 877
Cardelli J. A., Clayton G. C., Mathis J. S., 1989, ApJ, 345, 245
Ciardullo R., 2012, Ap&SS, 341, 151
Ciardullo R., 2013, in de Grijs R., ed., Proc. IAU Symp. 289, Advancing the Physics of Cosmic Distances. Kluwer, Dordrecht, p. 247
Ciardullo R., Jacoby G. H., Ford H. C., Neill J. D., 1989a, ApJ, 339, 53
Ciardullo R., Jacoby G. H., Ford H. C., 1989b, ApJ, 344, 715
Ciardullo R., Jacoby G. H., Tonry J. L., 1993, ApJ, 419, 479
Ciardullo R., Feldmeier J. J., Jacoby G. H., Kuzio de Naray R., Laychak M. B., Durrell P. R., 2002, ApJ, 577, 31
Courtois H. M., Tully R. B., 2012, ApJ, 749, 174
Davis B. D., Ciardullo R., Feldmeier J. J., Jacoby G. H., 2018, Research Notes of the American Astronomical Society, 2, 32
de Vaucouleurs G., de Vaucouleurs A., Buta R., Ables H. D., Hewitt A. V., 1981a, PASP, 93, 36
de Vaucouleurs G., Peters W. L., Bottinelli L., Gouguenheim L., Paturel G., 1981b, ApJ, 248, 408
den Brok M. et al., 2020, MNRAS, 491, 4089
Dhungana G. et al., 2016, ApJ, 822, 6
Dolphin A. E., Kennicutt, Robert C. J., 2002, AJ, 123, 207
Dopita M. A., Evans I. N., 1986, ApJ, 307, 431
Dopita M. A., Jacoby G. H., Vassiliadis E., 1992, ApJ, 389, 27
Ekholm T., Lanoix P., Teerikorpi P., Fouqué P., Paturel G., 2000, A&A, 355, 835
Emsellem E. et al., 2021, preprint (arXiv:2110.03708)
Feldmeier J. J., Ciardullo R., Jacoby G. H., 1997, ApJ, 479, 231
Feldmeier J. J., Jacoby G. H., Phillips M. M., 2007, ApJ, 657, 76
Ferrarese L. et al., 2000a, ApJS, 128, 431
Ferrarese L. et al., 2000b, ApJ, 529, 745
Folatelli G. et al., 2013, ApJ, 773, 53
Ford H. C., Jenner D. C., 1978, in BAAS. p. 665
Foreman-Mackey D., 2014, Blog post: Mixture models. Zenodo, available at https://doi.org/10.5281/zenodo.15856
Franchetti N. A. et al., 2012, AJ, 143, 85
Freedman W. L., 2021, ApJ, 919, 16
Freedman W. L. et al., 2001, ApJ, 553, 47
Fusco T. et al., 2020, A&A, 635, A208
Gadotti D. A. et al., 2019, MNRAS, 482, 506
Gaia Collaboration, 2018, A&A, 616, A1
Galán-de Anta P. M. et al., 2021, A&A, 652, A109
Georgiev T. B., Bilkina B. I., Dencheva N. M., 1997, Astronomy Letters, 23, 644
Giraud E., 1985, A&A, 153, 125
Grevesse N., Noels A., Sauval A. J., 1996, in Holt S. S., Sonneborn G., eds, ASP Conf. Ser. Vol. 99, Cosmic Abundances. Astron. Soc. Pac., San Francisco, p. 117
Harris C. R. et al., 2020, Nature, 585, 357
Hartke J., Arnaboldi M., Longobardi A., Gerhard O., Freeman K. C., Okamura S., Nakata F., 2017, A&A, 603, A104
Hendry M. A. et al., 2005, MNRAS, 359, 906
Herrmann K. A., Ciardullo R., Feldmeier J. J., Vinciguerra M., 2008, ApJ, 683, 630
Hoeflich P. et al., 2017, ApJ, 846, 58
Hogg D. W., Bovy J., Lang D., 2010, preprint (arXiv:1008.4686)
Howell S. B., 1989, PASP, 101, 616
Hunter J. D., 2007, Computing in Science & Engineering, 9, 90
Jacobs B. A., Rizzi L., Tully R. B., Shaya E. J., Makarov D. I., Makarova L., 2009, AJ, 138, 332
Jacoby G. H., 1989, ApJ, 339, 39
Jacoby G. H., 1997, in Livio M., Donahue M., Panagia N., eds, The Extragalactic Distance Scale. p. 197, preprint (arXiv:astro-ph/9608128)
Jacoby G. H., Ciardullo R., Harris W. E., 1996, ApJ, 462, 1
Jang I. S., Lee M. G., 2014, ApJ, 792, 52
Jang I. S., Lee M. G., 2017, ApJ, 836, 74

Jang I. S. et al., 2018, ApJ, 852, 60
Jha S., Riess A. G., Kirshner R. P., 2007, ApJ, 659, 122
Kanbur S. M., Ngeow C., Nikolaev S., Tanvir N. R., Hendry M. A., 2003, A&A, 411, 361
Karachentsev I. D., Makarov D. I., Kaisina E. I., 2013, AJ, 145, 101
Karachentsev I. D., Makarova L. N., Tully R. B., Rizzi L., Karachentseva V. E., Shaya E. J., 2017, MNRAS, 469, L113
Kourkchi E., Tully R. B., 2017, ApJ, 843, 16
Kourkchi E., Courtois H. M., Graziani R., Hoffman Y., Pomarède D., Shaya E. J., Tully R. B., 2020, AJ, 159, 67
Kreckel K., Groves B., Bigiel F., Blanc G. A., Kruijssen J. M. D., Hughes A., Schruba A., Schinnerer E., 2017, ApJ, 834, 174
Kreckel K. et al., 2019, ApJ, 887, 80
Kreckel K. et al., 2020, MNRAS, 499, 193
Kwok S., 2005, Journal of Korean Astronomical Society, 38, 271
Lagattuta D. J., Mould J. R., Staveley-Smith L., Hong T., Springob C. M., Masters K. L., Koribalski B. S., Jones D. H., 2013, ApJ, 771, 88
Lang P. et al., 2020, ApJ, 897, 122
Lee M. G., Freedman W. L., Madore B. F., 1993, ApJ, 417, 553
Lee M. G., Jang I. S., 2013, ApJ, 773, 13
Leroy A. et al., 2021, ApJS, 257, 43
Li L., Shen S., Hou J., Yuan H., Xiang M., Chen B., Huang Y., Liu X., 2018, ApJ, 858, 75
Longobardi A., Arnaboldi M., Gerhard O., Coccato L., Okamura S., Freeman K. C., 2013, A&A, 558, A42
Mandel K. S., Narayan G., Kirshner R. P., 2011, ApJ, 731, 120
McQuinn K. B. W., Skillman E. D., Dolphin A. E., Berg D., Kennicutt R., 2017, AJ, 154, 51
Méndez R. H., Riffeser A., Kudritzki R. P., Matthias M., Freeman K. C., Arnaboldi M., Capaccioli M., Gerhard O. E., 2001, ApJ, 563, 135
Müller T., Prieto J. L., Pejcha O., Clocchiatti A., 2017, ApJ, 841, 127
Nasonova O. G., de Freitas Pacheco J. A., Karachentsev I. D., 2011, A&A, 532, A104
Nugent P. et al., 2006, ApJ, 645, 841
Olivares E. F. et al., 2010, ApJ, 715, 833
Osterbrock D. E., Ferland G. J., 2006, Astrophysics of gaseous nebulae and active galactic nuclei. University Science Books, Sausalito, CA
Paturel G., Teerikorpi P., 2006, A&A, 452, 423
Pedreros M., Madore B. F., 1981, ApJS, 45, 541
Pejcha O., Prieto J. L., 2015, ApJ, 799, 215
Pilyugin L. S., Grebel E. K., 2016, MNRAS, 457, 3678
Pilyugin L. S., Grebel E. K., Kniazev A. Y., 2014, AJ, 147, 131
Polshaw J. et al., 2015, A&A, 580, L15
Poznanski D. et al., 2009, ApJ, 694, 1067
Reindl B., Tammann G. A., Sandage A., Saha A., 2005, ApJ, 624, 532
Riess A. G., Press W. H., Kirshner R. P., 1996, ApJ, 473, 88
Riess A. G. et al., 2016, ApJ, 826, 56
Rizzi L., Tully R. B., Makarov D., Makarova L., Dolphin A. E., Sakai S., Shaya E. J., 2007, ApJ, 661, 815
Rodríguez Ó., Clocchiatti A., Hamuy M., 2014, AJ, 148, 107
Roth M. M., Jacoby G. H., Ciardullo R., Davis B. D., Chase O., Weilbacher P. M., 2021, preprint (arXiv:2105.01982)
Rousseau-Nepton L. et al., 2019, MNRAS, 489, 5530
Roy R. et al., 2011, ApJ, 736, 76
Ruiz-Lapuente P., 1996, ApJ, 465, L83
Russell D. G., 2002, ApJ, 565, 681
Sabbi E. et al., 2018, ApJS, 235, 23
Saha A., Thim F., Tammann G. A., Reindl B., Sand age A., 2006, ApJS, 165, 108
Sakai S., Ferrarese L., Kennicutt, Robert C. J., Saha A., 2004, ApJ, 608, 42
Santoro F. et al., 2022, A&A, 658, A188
Schlafly E. F., Finkbeiner D. P., 2011, ApJ, 737, 103
Schmidt B. P., Kirshner R. P., Eastman R. G., 1992, ApJ, 395, 366
Schmidt B. P., Kirshner R. P., Eastman R. G., Phillips M. M., Suntzeff N. B., Hamuy M., Maza J., Aviles R., 1994, ApJ, 432, 42
Schoeniger F., Sofue Y., 1997, A&A, 323, 14
Schönberner D., Jacob R., Steffen M., Perinotto M., Corradi R. L. M., Acker A., 2005, A&A, 431, 963
Schönberner D., Jacob R., Sandin C., Steffen M., 2010, A&A, 523, A86
Sharina M. E., Karachentsev I. D., Tikhonov N. A., 1996, A&AS, 119, 499
Shaver P. A., McGee R. X., Newton L. M., Danks A. C., Pottasch S. R., 1983, MNRAS, 204, 53
Shaya E. J., Tully R. B., Hoffman Y., Pomarède D., 2017, ApJ, 850, 207
Sohn Y.-J., Davidge T. J., 1996, AJ, 111, 2280
Sorce J. G., Tully R. B., Courtois H. M., 2012, ApJ, 758, L12
Sorce J. G., Tully R. B., Courtois H. M., Jarrett T. H., Neill J. D., Shaya E. J., 2014, MNRAS, 444, 527
Sparks W. B., 1994, ApJ, 433, 19
Spriggs T. W. et al., 2020, A&A, 637, A62
Spriggs T. W. et al., 2021, A&A, 653, A167
Springob C. M., Haynes M. P., Giovanelli R., Kent B. R., 2005, ApJS, 160, 149
Springob C. M., Masters K. L., Haynes M. P., Giovanelli R., Marinoni C., 2009, ApJS, 182, 474
Stetson P. B., 1987, PASP, 99, 191
Takanashi N., Doi M., Yasuda N., 2008, MNRAS, 389, 1577
Tammann G. A., Sandage A., Reindl B., 2008, A&A Rev., 15, 289
Teodorescu A. M., Méndez R. H., Bernardi F., Thomas J., Das P., Gerhard O., 2011, ApJ, 736, 65
Terry J. N., Paturel G., Ekholm T., 2002, A&A, 393, 57
Theureau G., Hanski M. O., Coudreau N., Hallet N., Martin J. M., 2007, A&A, 465, 71
Tonry J. L., Dressler A., Blakeslee J. P., Ajhar E. A., Fletcher A. B., Luppino G. A., Metzger M. R., Moore C. B., 2001, ApJ, 546, 681
Toribio San Cipriano L., Domínguez-Guzmán G., Esteban C., García-Rojas J., Mesa-Delgado A., Bresolin F., Rodríguez M., Simón-Díaz S., 2017, MNRAS, 467, 3759
Tully R. B., Fisher J. R., 1988, Catalog of Nearby Galaxies. Cambridge Univ. Press, Cambridge
Tully R. B., Rizzi L., Shaya E. J., Courtois H. M., Makarov D. I., Jacobs B. A., 2009, AJ, 138, 323
Tully R. B. et al., 2013, AJ, 146, 86
Tully R. B., Courtois H. M., Sorce J. G., 2016, AJ, 152, 50
Van Dyk S. D., Li W., Filippenko A. V., 2006, PASP, 118, 351
Van Dyk S. D. et al., 2015, ApJ, 806, 195
Ventimiglia G., Arnaboldi M., Gerhard O., 2011, A&A, 528, A24
Weilbacher P. M. et al., 2020, A&A, 641, A28
Westfall K. B. et al., 2019, AJ, 158, 231
Willick J. A., Courteau S., Faber S. M., Burstein D., Dekel A., Strauss M. A., 1997, ApJS, 109, 333
Yasuda N., Fukugita M., Okamura S., 1997, ApJS, 108, 417
Zasov A. V., Bizyaev D. V., 1996, Astronomy Letters, 22, 71
Zhang J.-J., Wang X.-F., Bai J.-M., Zhang T.-M., Wang B., Liu Z.-W., Zhao X.-L., Chen J.-C., 2014, AJ, 148, 1

SUPPORTING INFORMATION

Supplementary data are available at *MNRAS* online.

Table 2. Planetary nebula identifications and supernova remnant contaminants.

Please note: Oxford University Press is not responsible for the content or functionality of any supporting materials supplied by the authors. Any queries (other than missing material) should be directed to the corresponding author for the article.

APPENDIX A: COMPARISON WITH LITERATURE DISTANCES

In Figs A1 to A18, we compare our measured distances with literature values. The data for the plots were taken from the NASA/IPAC

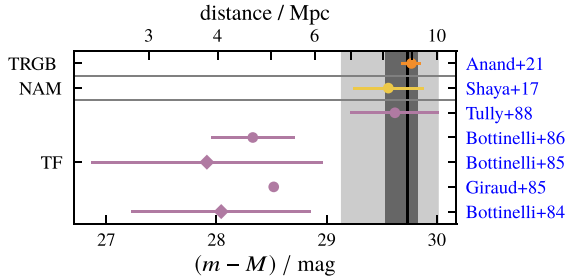

Figure A1. Same as Fig. 8, but for IC 5332. We measure a distance modulus of $(m - M) = 29.73^{+0.10}_{-0.20}$ mag ($D = 8.84^{+0.39}_{-0.82}$ Mpc).

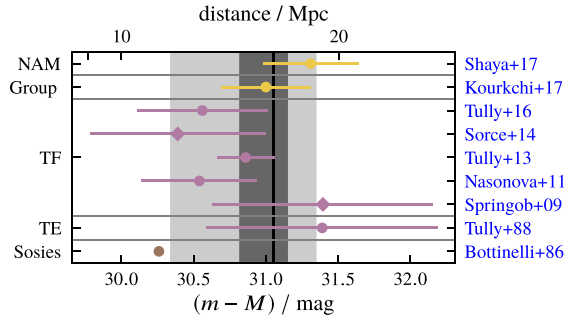

Figure A2. Same as Fig. 8, but for NGC 1087. We measure a distance modulus of $(m - M) = 31.05^{+0.10}_{-0.24}$ mag ($D = 16.25^{+0.74}_{-1.79}$ Mpc).

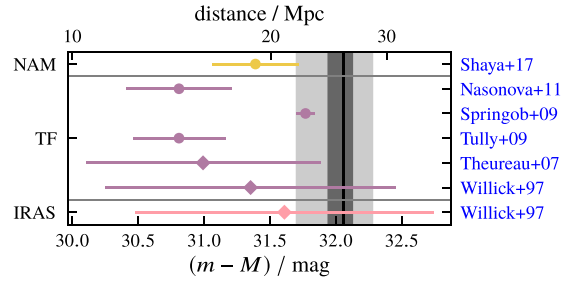

Figure A3. Same as Fig. 8, but for NGC 1300. We measure a distance modulus of $(m - M) = 32.06^{+0.08}_{-0.12}$ mag ($D = 25.77^{+0.90}_{-1.42}$ Mpc).

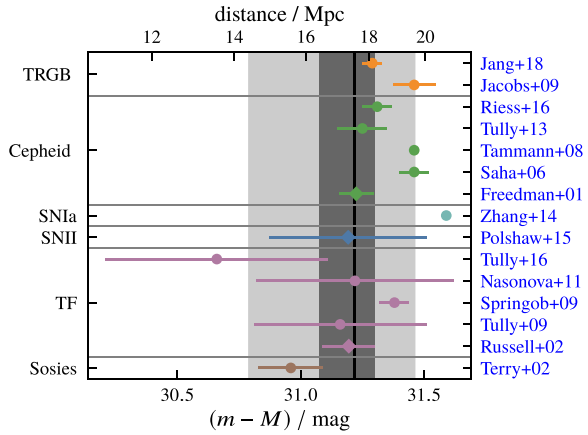

Figure A4. Same as Fig. 8, but for NGC 1365. We measure a distance modulus of $(m - M) = 31.22^{+0.08}_{-0.14}$ mag ($D = 17.53^{+0.66}_{-1.16}$ Mpc).

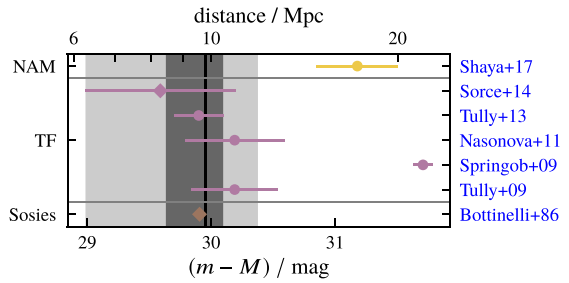

Figure A5. Same as Fig. 8, but for NGC 1385. We measure a distance modulus of $(m - M) = 29.96^{+0.14}_{-0.32}$ mag ($D = 9.81^{+0.63}_{-1.46}$ Mpc).

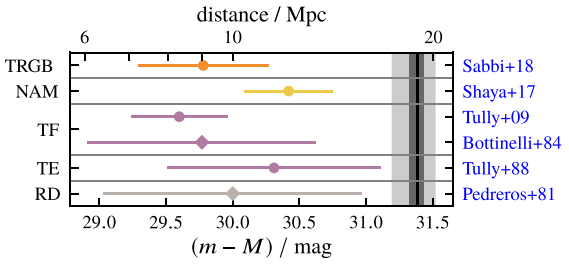

Figure A6. Same as Fig. 8, but for NGC 1433. We measure a distance modulus of $(m - M) = 31.39^{+0.04}_{-0.07}$ mag ($D = 18.94^{+0.39}_{-0.56}$ Mpc).

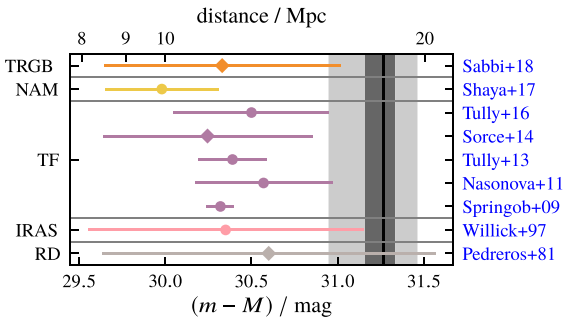

Figure A7. Same as Fig. 8, but for NGC 1512. We measure a distance modulus of $(m - M) = 31.27^{+0.07}_{-0.11}$ mag ($D = 17.93^{+0.53}_{-0.88}$ Mpc).

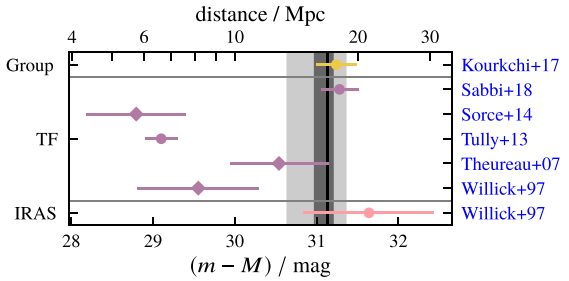

Figure A8. Same as Fig. 8, but for NGC 1566. We measure a distance modulus of $(m - M) = 31.13^{+0.08}_{-0.17}$ mag ($D = 16.84^{+0.60}_{-1.29}$ Mpc).

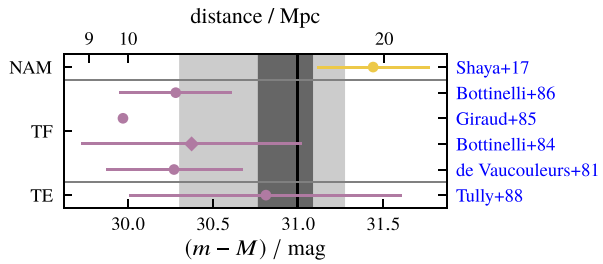

Figure A9. Same as Fig. 8, but for NGC 1672. We measure a distance modulus of $(m - M) = 30.99^{+0.09}_{-0.23}$ mag ($D = 15.80^{+0.68}_{-1.68}$ Mpc).

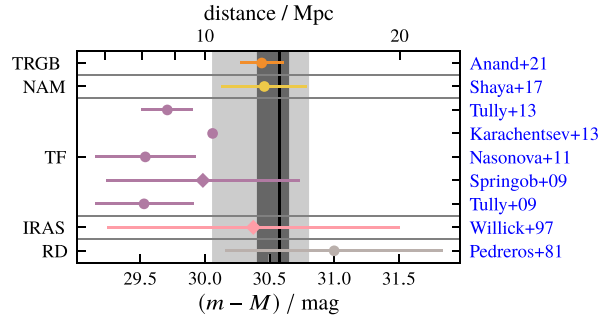

Figure A10. Same as Fig. 8, but for NGC 2835. We measure a distance modulus of $(m - M) = 30.57^{+0.08}_{-0.17}$ mag ($D = 13.03^{+0.46}_{-1.04}$ Mpc).

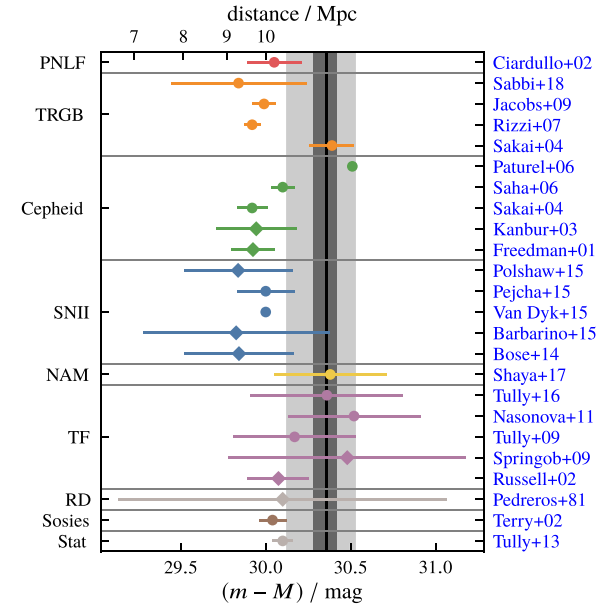

Figure A11. Same as Fig. 8, but for NGC 3351 (M 95). We measure a distance modulus of $(m - M) = 30.36^{+0.06}_{-0.08}$ mag ($D = 11.80^{+0.31}_{-0.43}$ Mpc).

Extragalactic Database (NED).[4] If a source published more than one distance, the mean of the published distances is used with the uncertainties added in quadrature (those values are marked with a diamond). Only the five most recent publications are considered for each method. The Numerical action method (NAM) distances were obtained by Anand et al. (2021) with the online tool[5] by Kourkchi et al. (2020) and Shaya et al. (2017).

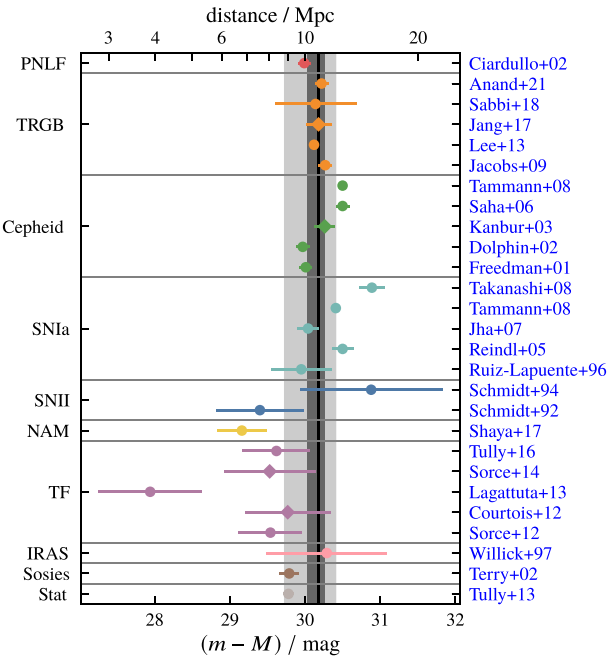

Figure A12. Same as Fig. 8, but for NGC 3627 (M 66). We measure a distance modulus of $(m - M) = 30.18^{+0.08}_{-0.15}$ mag ($D = 10.88^{+0.39}_{-0.77}$ Mpc).

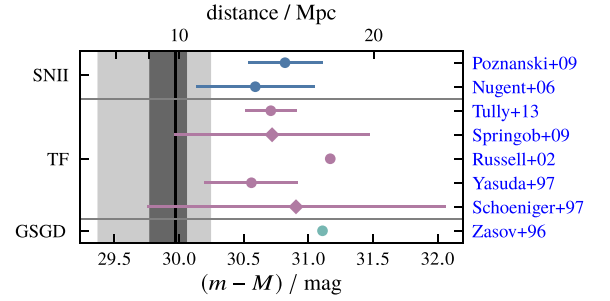

Figure A13. Same as Fig. 8, but for NGC 4254 (M 99). We measure a distance modulus of $(m - M) = 29.97^{+0.09}_{-0.20}$ mag ($D = 9.86^{+0.42}_{-0.91}$ Mpc).

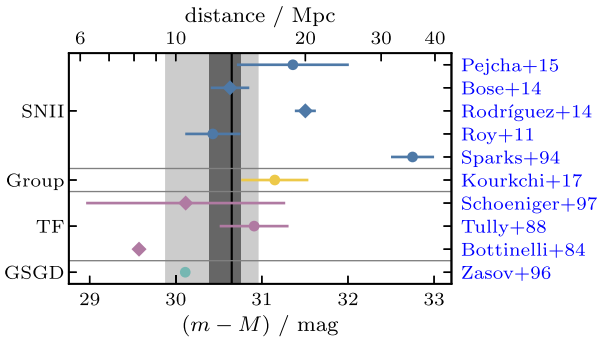

Figure A14. Same as Fig. 8, but for NGC 4303 (M 61). We measure a distance modulus of $(m - M) = 30.65^{+0.10}_{-0.26}$ mag ($D = 13.49^{+0.64}_{-1.60}$ Mpc).

[4] https://ned.ipac.caltech.edu/Library/Distances/

[5] http://edd.ifa.hawaii.edu/NAMcalculator/

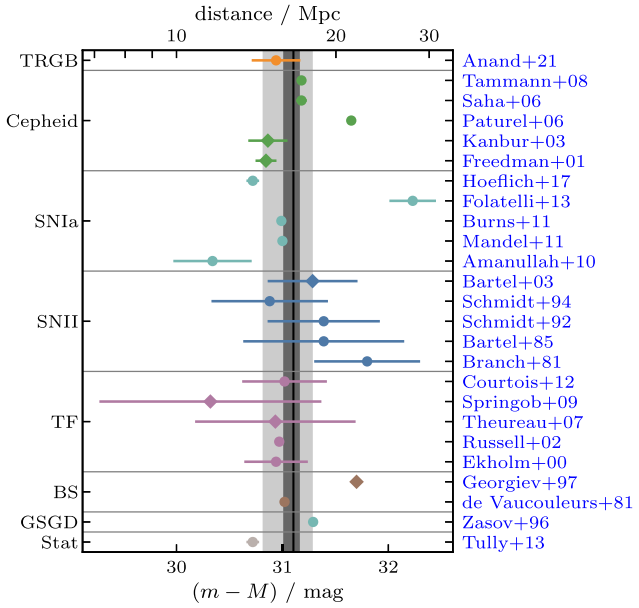

Figure A15. Same as Fig. 8, but for NGC 4321 (M 100). We measure a distance modulus of $(m - M) = 31.10^{+0.06}_{-0.10}$ mag ($D = 16.62^{+0.46}_{-0.74}$ Mpc).

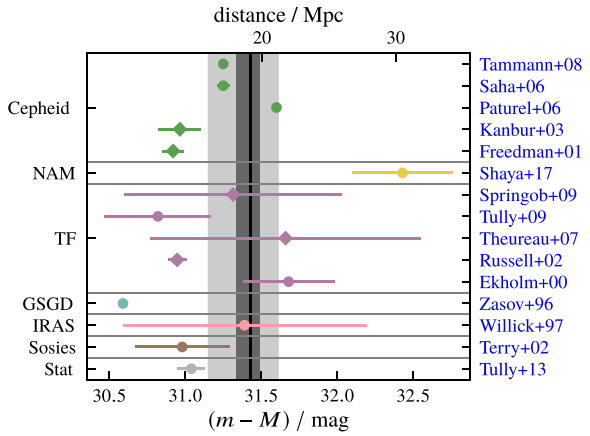

Figure A16. Same as Fig. 8, but for NGC 4535. We measure a distance modulus of $(m - M) = 31.43^{+0.06}_{-0.09}$ mag ($D = 19.29^{+0.56}_{-0.82}$ Mpc).

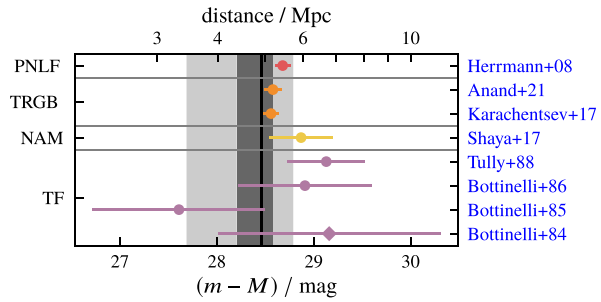

Figure A17. Same as Fig. 8, but for NGC 5068. We measure a distance modulus of $(m - M) = 28.46^{+0.11}_{-0.26}$ mag ($D = 4.93^{+0.24}_{-0.59}$ Mpc).

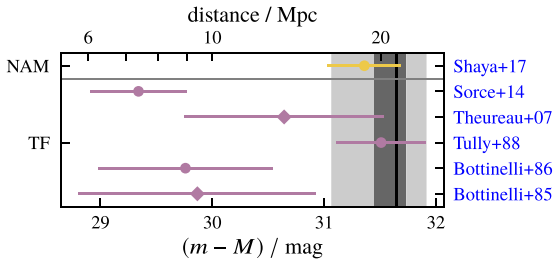

Figure A18. Same as Fig. 8, but for NGC 7496. We measure a distance modulus of $(m - M) = 31.64^{+0.09}_{-0.19}$ mag ($D = 4.93^{+0.24}_{-0.59}$ Mpc).

We use the following abbreviations in the figures: Planetary Nebula Luminosity Function (PNLF), Tip of the Red Giant Branch (TRGB), Type Ia Supernova (SNIa), SNII optical (SNII), Numerical action method (NAM), distance to galaxy group (Group), Tully–Fisher (TF), Tully estimate (TE), Brightest Stars (BS), Gravitational Stability Gaseous Disc (GSGD), Disc Stability (DS), Infra-Red Astronomical Satellite (IRAS), Ring Diameter (RD) and Statistical (Stat).

APPENDIX B: EXTINCTION CORRECTION

To quantify if we can ignore the effects of internal extinction (dust within the target galaxy, not the circumstellar extinction of the PN itself), we create a synthetic luminosity function by sampling from equation (7). To half of the sample we randomly add extinction. Then we use our fitting algorithm to measure the distance to the sampled data. Fig. B1 shows the PNLF without extinction and with extinction. As shown in Appendix C, the ability to derive a reliable distance depends on the sample size and the range of the PNLF that we sample. For a sample size of 20 PNe, the measured distance is unaffected for $A_{5007} = 0.1$ mag, but can be significantly overestimated for $A_{5007} = 1$ mag. Once the sample gets larger, the impact decreases and for a sample size of 100 PNe, our algorithm is able to derive the correct distances from the compound sample with any A_{5007}.

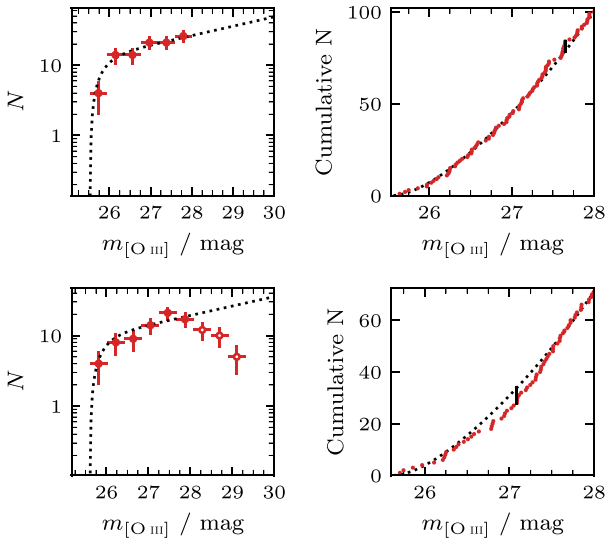

Figure B1. We synthesize a PNLF with 100 points. Half of the points are randomly chosen and an extinction of $A_{5007} = 1$ mag is applied. The top panels show the full sample without extinction and the bottom panels show the compound sample with the extinction applied. The left panels show the binned PNLF and the right panels show the cumulative PNLF.

As Fig. B1 shows, the composition of a luminosity function should bend the observed luminosity function below the fitted function. Since we do not observe this behaviour in our observed sample, this further indicates that our sample is not significantly reddened.

APPENDIX C: PRECISION OF THE PNLF

The fit of the PNLF is dominated by the brightest PNe. Once we observe a PNe with apparent magnitude $m_{[\mathrm{O\,III}]}$, the galaxy can not be further away than $(m - M)_{\mathrm{max}} = m_{[\mathrm{O\,III}]} - M^*$, where M^* is the zero-point of the PNLF (it can be slightly further away due to the way we include the uncertainties with equation 9). Due to the exponential tail of the PNLF, the fainter PNe push the function to the right (e.g. towards larger distances). Hence if we only observe the bright end, we usually underestimate the distance.

Jacoby (1997) investigated the effects of sample size by measuring the PNLF from different sized subsets from the PNe detected in M 87. To test the reliability of the PNLF, we do something similar with synthetic data. We vary the sample size from 20 to 150 objects and the completeness limit from 26.5 to 28 mag. For each step we sample 1000 luminosity functions with a fixed distance modulus of $(m - M) = 30$ mag. The later means that the part of the PNLF that we sample varies from 1.0 to 2.5 mag. The result can be seen in Fig. C1. The precision increases with sample size, showing that even from a small sample of 20 PNe, one can achieve a precision better than ~ 5 per cent. For a brighter completeness limit, the sample is concentrated at the steep cut-off, and hence the distance is very well constrained. For fainter completeness limits, this part is sampled more sparsely which leads to a lower precision of the measured distance.

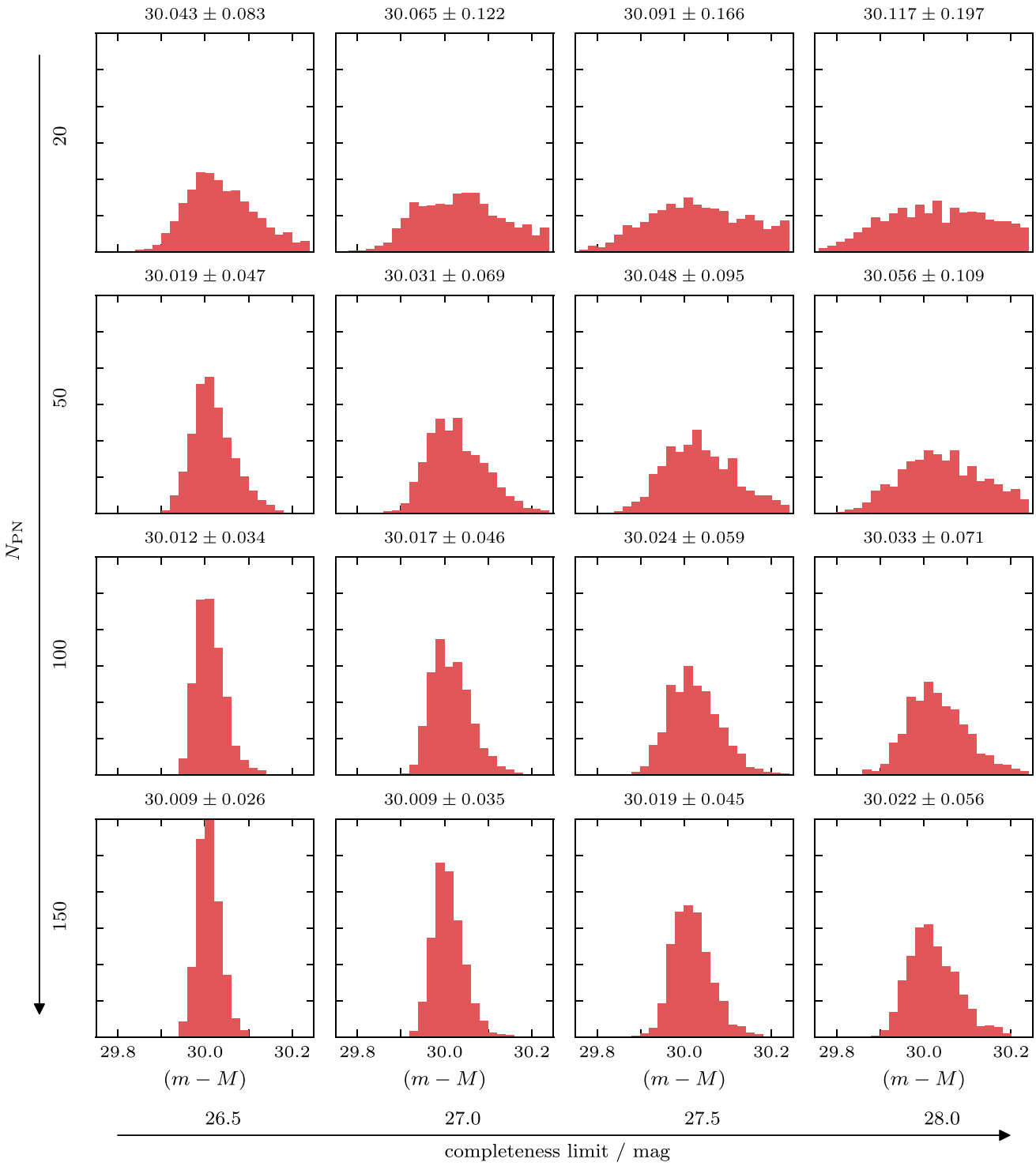

Figure C1. A demonstration of the precision that can be achieved with the PNLF, depending on the sample size and part of the PNLF that is sampled. We sample the PNLF for a distance modulus of $(m - M) = 30$ mag. The sample size $N_{\rm PN}$ increases from 20, 50, 100 to 150 and the completeness limit increases from 26.5 to 28 mag in 0.5 mag increments (meaning that we sample 1.0 to 2.5 mag of the PNLF). The precision increases with sample size and even a small sample of 20 PNe is enough to achieve a precision around 5 per cent. When we only sample a small part of the luminosity function, the sample is concentrated at the bright cut-off and the distance is well constrained. With a fainter completeness limit, the sample is distributed more and the more sparsely sampled cut-off yields a less precise distance.

This paper has been typeset from a TEX/LATEX file prepared by the author.